

# The zero problem: Gaussian process emulators for range constrained computer models

Elaine T. Spiller\*, Robert L. Wolpert<sup>†</sup>, Pablo Tierz<sup>‡</sup>, and Taylor G. Asher<sup>§</sup>

**Abstract.** We introduce a zero-censored Gaussian process as a systematic, model-based approach to building Gaussian process emulators for range-constrained simulator output. This approach avoids many pitfalls associated with modeling range-constrained data with Gaussian processes. Further, it is flexible enough to be used in conjunction with statistical emulator advancements such as emulators that model high-dimensional vector-valued simulator output. The zero-censored Gaussian process is then applied to two examples of geophysical flow inundation which have the constraint of non-negativity.

**Key words.** Gaussian processes, statistical surrogates, censored data, geophysical flows

**AMS subject classifications.** 60G15, 86-08, 62N01

**1. Introduction.** Gaussian process based surrogates of computationally intensive models have become an essential class of tools for uncertainty quantification since the seminal papers led by Currin, Sacks, and Welch (Currin et al., 1988; Sacks et al., 1989b,a; Welch et al., 1992). The flexibility of Gaussian processes to model computationally intensive problems from a wide breadth of applications is remarkable. One challenging class of problems are computer models whose output range is constrained by minimum and/or maximum values. A common subset of these problems are computer models whose output is positive or zero. This “zero problem” poses great challenges in fitting Gaussian process emulators (GPs). To start, data with large numbers of zeros are not naturally modeled by Gaussian probability density functions due to their full support. Yet it is advantageous to leverage the vast body of work over the last few decades – both theory and techniques – on emulating simulators with Gaussian processes. As such we introduce a simulation based strategy to model bounded computer model output that addresses the semi-binary nature of the data and results in a GP model with full support. For the case of nonnegative data taking the value zero with positive probability, our approach begins by modeling the data as the maximum of zero and a latent Gaussian process. The challenge remaining is to find or approximate the intractable posterior distribution of that latent GP given the data.

An interesting and important class of models that suffer from the “zero problem” are geophysical flows. Consider inundation from tsunamis, volcanic flows, storm surge, etc. A given computer model run, representing one possible scenario, of any of these processes, will output the depth of inundation over a spatial region of interest. Such simulations are computationally intensive, taking minutes to days to complete a single simulator run on a super computer.

---

\*Department of Mathematical and Statistical Sciences, Marquette University, Milwaukee, WI, USA (elaine.spiller@marquettet.edu).

<sup>†</sup>Department of Statistical Science, Duke University, Durham, NC, USA.

<sup>‡</sup>British Geological Survey, The Lyell Centre, Edinburgh, UK, and The School of Geosciences, University of Edinburgh, Edinburgh, UK.

<sup>§</sup>Department of Earth, Marine, and Environmental Sciences, University of North Carolina, Chapel Hill, NC, USA.

Hazard analysis or hazard forecasting typically relies on Bayesian simulation-based inference methods that require thousands to millions of simulation runs. Given these constraints, hazard analysis is nearly infeasible using full model evaluation of the simulator. Likewise exploring hazard analyses under various potential aleatory scenarios and/or quantifying epistemic uncertainties in such analyses with direct computer model evaluations is intractable. As such, computationally efficient surrogate models that can address the “zero-problem” have the potential to greatly advance the field of geophysical hazard analysis.

For simulators with vector-valued outputs that are range constrained, the full support of Gaussian processes is not the only challenge for emulation. In particular, the regions of input space that lead zero-output can (and often do) differ for each element of the output vector. In the context of geophysical flows, the boundary in scenario space that leads to zero output or positive output, varies spatially among output map nodes (point of interest inside the hazard domain). Consider a batch of simulator runs covering a wide range of potential scenarios, here each element of the vector-valued output element represents a map node. Further, each will have its own set of runs resulting in positive inundation and set of runs resulting in no inundation. Clearly this kind of model output data is non-stationary, but has the added challenge that the non-stationarity is indicated by a discontinuity in the derivative of the GP.

Our group and others have made significant advances in GP-based probabilistic hazard assessment, probabilistic hazard forecasting, and probabilistic hazard mapping over the last decade (Bayarri et al., 2009, 2015; Beck and Guillas, 2016; Jia et al., 2016; Liu and Guillas, 2017; Rutarindwa et al., 2019). These various works address the large-dimensional spatial nature of the output by fitting emulators independently, by applying partial-parallel emulation (PPE), or by fitting emulators to coefficients of basis functions or principal components (GP-PCA) (Spiller et al., 2014; Gu and Berger, 2016; Higdon et al., 2008). In this work, we do not advocate for a particular choice of handling high-dimensional output, but instead provide a solution to the zero problem that will be suitable to work with any of these techniques. Various previous approaches to the zero problem in the works cited in this paragraph include: trying to ignore it; focusing on spatial regions that are inundated under every scenario; inputting missing (zero) data via spatial interpolation; including only a subset of zeros that are nearest in design space to simulations resulting in positive output at a given node. All of these approaches are rather ad-hoc (although some work quite well) and this particular form of non-stationarity remains a significant challenge for GP emulator-based geophysical hazard analysis.

Several GP emulation methods have been proposed to handle non-stationarity and/or discontinuous data. Many of these approaches are based on partitioning the input space and then either fitting separate GPs to the different regions or taking mixtures of input-region specific kernels to fit the GP (Gramacy and Lee, 2008; Pope et al., 2019; Volodina and Williamson, 2020). Yet for the zero problem, such a partition of input space would necessarily differ for each map node as the set of zero outputs varies spatially. Even if one could automate map node specific partitions, it is not clear how global emulator approaches – like parallel partial emulation or GPs fit to PCA modes – could be applied. Instead, we model the data as the maximum of zero and a latent GP and then, for each map node, we consider imputing negative GP values at design points whose output is zero, from a conditional distribution consistent with the simulator data. Once this preprocessing step is complete, the new partially-imputed model design and response set will fit assumptions needed for any

80 of the high-dimensional GP output emulator approaches. As such the imputation approach  
 81 employed by the zero-constrained Gaussian process is an *enabling technology* – it allows GP  
 82 emulation, and variations to fit large-dimensional spatial output, of geophysical models that  
 83 GP emulators are otherwise poorly suited to model.

84 There are several recent approaches to developing range constrained GPs in the computer  
 85 modeling community which are largely inspired by the geostatistics paper on kriging with  
 86 inequality constraints (Abrahamsen and Benth, 2001). There are two general approaches  
 87 taken, the first of which relies on choosing constrained basis functions or constrained splines  
 88 and modeling the associated coefficients with (truncated) Gaussian processes (Ben Salem et al.,  
 89 2019; López-Lopera et al., 2018; Maatouk and Bay, 2017; Swiler et al., 2020). The common  
 90 thread of the second approach is to fit all available model data and impute a set of “artificial  
 91 data” throughout the input space points that maintain the constraint. These auxiliary data  
 92 are subsequently used for fitting Gaussian processes (Agrell, 2019; Wang and Berger, 2016;  
 93 Da Veiga and Marrel, 2012, 2020). One other recent work sets up the constrained optimization  
 94 problem to optimize range parameters under a slightly-relaxed constraint that the predictive  
 95 GP obeys the range constraint at untested inputs with high probability (Pensoneault et al.,  
 96 2020). Some ideas of censored GPs are explored in (Kzyurova, 2017), but are undeveloped. In  
 97 this work we propose an approach that addresses the non-stationary nature of semi-binary data  
 98 and that can be readily “plugged-in” to existing GP approaches that handle high-dimensional  
 99 output.

100 Because of the non-negativity constraint we cannot take a surrogate to have a multivariate  
 101 Normal distribution, but we can still leverage the vast development of Gaussian Process  
 102 technology by constructing a surrogate of computer model output that takes on the maximum  
 103 of zero and a GP that is constrained to fit the positive output data. Again, we refer to such  
 104 a process as a *zero-censored Gaussian Process*, or “zGP.” After introducing notation and  
 105 GP basics, we go through the zGP construction noting important details for successful and  
 106 efficient algorithm implementation including the choice of mean trend, initialization, and zGP  
 107 parameterization that uses “zero” information and captures uncertainty in the modeling due to  
 108 imputation. We then demonstrate the zGP’s efficacy by applying it to two different hazardous  
 109 geophysical flows: storm surge and granular volcanic flows.

## 110 2. Background.

111 **2.1. Gaussian Process Emulation.** In the simplest sense, Gaussian process emulation can  
 112 be thought of as a statistical model of a complicated and computationally intensive physical  
 113 model. The idea is to treat the computer model response as coming from a random function  
 114 in the class of weakly stationary Gaussian processes. To do so, we will only consider random  
 115 functions that are conditioned on going through (or near) the computer model output data.  
 116 Determining parameters of a GP that are consistent with the computer model response is  
 117 described as “fitting” the GP. Once the GP model is determined, one can replace the com-  
 118 putationally intensive computer model simulations with a function evaluation (Welch et al.,  
 119 1992; Santner et al., 2018).

120 Starting with notation, let  $\mathbf{x}$  be a  $p$ -dimensional vector of inputs to the computer model,  
 121 lying in a domain  $\mathcal{X} \subseteq \mathbb{R}^p$  of possible values – so  $\mathbf{x} = (x_1, \dots, x_p)^\top \in \mathcal{X} \subseteq \mathbb{R}^p$ . This vector is  
 122 typically comprised of initial conditions, parameters, and/or boundary conditions needed to

123 specify completely a single computer model run. In the context of inundation from geophysical  
 124 flows, the input vector would represent one possible scenario. Likewise, we will denote the  
 125 computer model output as  $y^M(\mathbf{x})$  – for the applications explored in this work, that is the  
 126 (necessarily nonnegative) maximum depth of flow inundation from a geophysical simulation for  
 127 the scenario characterized by  $\mathbf{x}$ . Consider  $n$  space-filling computer model runs, *i.e.*,  $n$  scenarios  
 128 (indexed by  $j \in J$ ) typically called the *design*, and denote that design as  $\mathcal{D} = \{\mathbf{x}_j : j \in J\}$ .  
 129 The output from all design runs is taken together as  $\mathbf{y}^M = (y_1^M, \dots, y_n^M)^\top \in \mathbb{R}^n$ . Lastly, we  
 130 will denote the resulting design input-output pairs as  $\mathcal{D}^M = \{(\mathbf{x}_j, y_j^M) : j \in J\}$ .

131 Now we will treat this computer model output data as a random vector with components  
 132  $y_j^M = Z_j$ , with  $\{Z_j \sim \text{No}(\mu, \Sigma) : j \in J\}$  where  $\mu_j = \mu(\mathbf{x}_j)$  is a known mean trend function  
 133 which may implicitly depend on uncertain parameters. The matrix,  $\Sigma = \sigma^2 \mathbf{R}$ , is an  $n \times n$   
 134 covariance matrix comparing the design points in  $\mathcal{D}$ . One can calculate  $(\mathbf{R})_{i,j} = c(\mathbf{x}_i, \mathbf{x}_j)$  using  
 135 a covariance function  $C(\cdot, \cdot) = \sigma^2 c(\cdot, \cdot)$  with scalar variance  $\sigma^2$ . Throughout this work, we  
 136 will utilize a separable Matérn 5/2 correlation function (see Stein (1999), §2.10) for arguments  
 137 supporting this choice). For two inputs  $\mathbf{x}_i = (x_{i1}, \dots, x_{ip})^\top$  and  $\mathbf{x}_j = (x_{j1}, \dots, x_{jp})^\top$ , the  
 138 standardized distance and correlation are:

$$(2.1) \quad d_k = \left( \frac{|x_{ik} - x_{jk}|^2}{\rho_k^2} \right)^{1/2}$$

$$c(\mathbf{x}_i, \mathbf{x}_j) = \prod_{k=1}^p \left( 1 + \sqrt{5}d_k + \frac{5}{3}d_k^2 \right) \exp(-\sqrt{5}d_k).$$

139 The *range parameters*  $\{\rho_k : k = 1, \dots, p\}$ , along with parameters describing the mean function  
 140  $\mu(\cdot)$  comprise the set of parameters needed to define a GP, and we call these parameters  $\theta$ .  
 141 With an estimate  $\hat{\theta} \approx \theta$  in hand (note hatted quantities represent estimates), we can generate  
 142 predictions of the computer model output at untried points (indexed by  $i \in I$ ) with

$$(2.2) \quad Z_I \sim \text{GP}(\mu_I, \Sigma_{II} \mid \mathcal{D}^M, \theta) = \text{GP}(m_{I|J}, V_{I|J})$$

143 with conditional mean vector and covariance matrix given by the usual Gaussian formulas:

$$(2.3) \quad m_{I|J} = \mathbb{E}[Z_I \mid \mathcal{D}^M, \theta] = \mu_I + \Sigma_{IJ} \Sigma_{JJ}^{-1} (Z_J - \mu_J)$$

$$(2.4) \quad V_{I|J} = \mathbb{E}[(Z_I - m_{I|J})(Z_I - m_{I|J})^\top \mid \mathcal{D}^M, \theta] = \Sigma_{II} - \Sigma_{IJ} \Sigma_{JJ}^{-1} \Sigma_{JI}$$

144 In practice we must use an estimate  $\hat{\theta} \approx \theta$ . Going forward, we will suppress the dependence  
 145 on  $\theta$  in our notation, and will sometimes let the  $I|J$  be implicit where no confusion arises.

146 The crux of this paper is adapting and applying this modeling strategy when the computer  
 147 model output data,  $\mathbf{y}^M$ , has range constraints. In particular, we will focus on the constraint  
 148 that the output data is non-negative, but the methodology we develop here would also apply  
 149 to other minimum and/or maximum value restrictions on the output data.

### 150 3. Methodology.

151 **3.1. Motivation.** Our two motivating applications are both geophysical flows that can  
 152 result in hazardous inundation, namely inundation due to storm surge and inundation due to

153 rapid granular volcanic flows known as pyroclastic density currents (PDCs). Both phenomena  
 154 are modeled by hyperbolic partial differential equations (PDEs) numerically solved over digital  
 155 elevation models (DEMs). Such computer models are computationally intensive, and a typical  
 156 simulation – depending on the scenario considered along with the desired accuracy of the solver  
 157 – can take hours to days to run on a high performance computing system (further details on  
 158 these computer models will be given in section 4). Another commonality between these  
 159 simulators is the complicated spatial footprints of inundation heights that result as output.  
 160 In Fig. 1 (left) we see the simulated spatial extent and maximum PDC flow depth (color) of  
 161 two different but typical simulations. Likewise in Fig. 1 (right) we see maximum storm surge  
 162 inundation for four different simulations (*i.e.*, four differently parameterized storms) at a set  
 163 of over-water and over-land map nodes. Of the 908 map nodes where storm surge depth is  
 164 reported, simulated storms labeled (a)–(d) in Fig. 1 yielded 382, 370, 237, and 290 zero-output  
 (or “dry”) nodes, respectively.

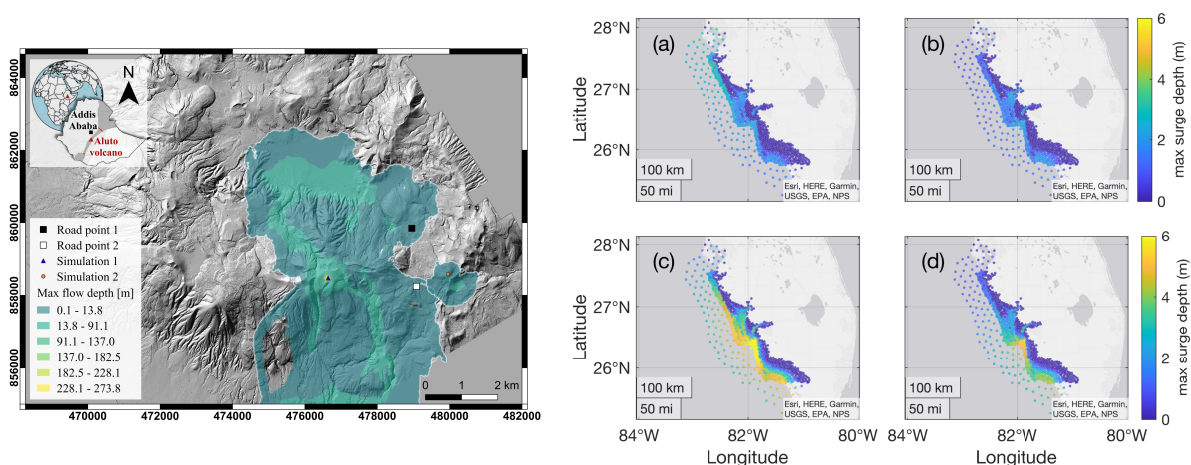


Figure 1: Left: Two simulated max PDC flow depths from flows that originate at different vent locations (blue triangle and orange circle) at Aluto volcano, Ethiopia (see simplified geographical context in the top-left corner of inset.) Note how the PDC simulation that originated at the blue triangle inundates both road points of interest (white and black squares) while the PDC simulation that originated at the orange circle almost inundates the white square road point, but does not come close to inundating the black square road point. Right: Four storms surge simulated max inundation depths on a grid of map nodes both overland and over water on the Southwest coast of Florida, USA. The darkest blue color indicate no inundation at those nodes.

165 Our strategy is to impute negative values for the zero-outputs that are consistent with GPs  
 166 fit to the positive model response. In particular, this approach readily distinguishes between  
 167 simulations that *almost inundate* a given node from those that do not. To elucidate the zGP  
 168 approach, we will explain and apply it to a scalar output illustrative example as we introduce  
 169 it.  
 170

171 **3.1.1. An illustrative example..** We begin with a pedagogical example to illustrate the  
 172 approach and introduce the necessary notation. We specify a deterministic function  $h$  on the  
 173 domain  $\mathcal{X} = [0, 1]^2 \subset \mathbb{R}^2$ , playing the role of a deterministic computer model with input space  
 174  $\mathcal{X}$ , and try to reconstruct it from a design set  $\mathcal{D}^M = \{\mathbf{x}_j, y_j : j \in J\}$  with  $y_j = h(\mathbf{x}_j)$ . We  
 175 begin with a slightly modified toy function of Bastos and O’Hagan (2009) shifted vertically,  
 176 given as  $h(\cdot) = 0 \vee f(\cdot)$ , where with  $\mathbf{x} = (x_1, x_2)$  and

$$(3.1) \quad f(\mathbf{x}) = \left(1 - \exp\left(-\frac{1}{2x_2}\right)\right) \left(\frac{2300x_1^3 + 199x_1^2 + 2092x_1 + 60}{100x_1^3 + 500x_1^2 + 4x_1 + 20}\right) - 6.$$

177 The toy function,  $h$ , along with  $n = 50$  Latin hypercube (LHC) design-response pairs, are  
 178 plotted in Fig. 2. Note for the design used in this example, there are 26 design points that  
 lead to a zero response and 24 that lead to a positive response.

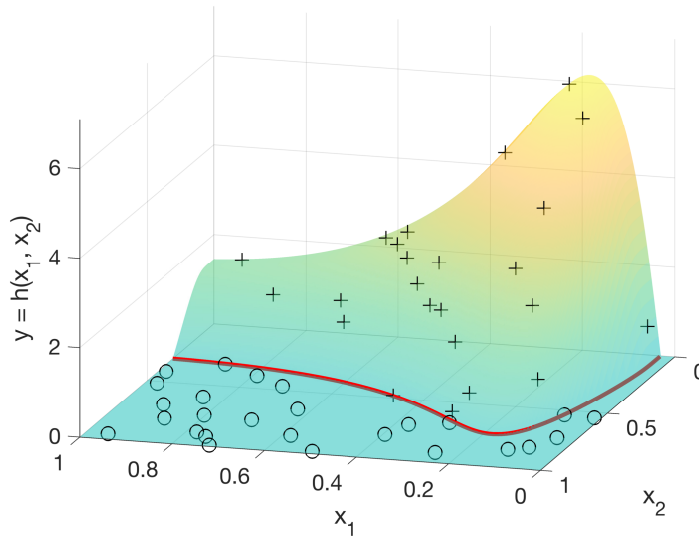


Figure 2: The non-negative function,  $h = 0 \vee f$ , plotted along with design points/responses that resulted in positive (+) and zero (o) model output. To add some contrast to the visualization, we have also included a red line indicating the zero-contour of  $f$ .

179

180 **3.2. Zero-censored Gaussian Process.** Again, our design consists of a finite set  $\mathcal{D} =$   
 181  $\{\mathbf{x}_j : j \in J\}$ , but we now consider the case where  $\mathcal{D}^M = \{(\mathbf{x}_j, y_j^M) : j \in J\}$  are ordered  
 182 pairs of observed nonnegative scalar output values,  $y_j^M \in \mathbb{R}_{\geq 0}$ , of a computer simulator at  
 183 model input vectors  $\mathbf{x}_j \in \mathcal{X} \subset \mathbb{R}^p$  ( $p = 2$  in the illustrative example), all indexed by a finite  
 184 set  $J$ . We can think of each input vector,  $\mathbf{x}_j$ , representing a distinct *model scenario* or one  
 185 choice of model inputs that parameterizes a particular realization of the simulator. The model  
 186 output is *strictly* positive for some number  $n_+ := |J_+|$  of indices  $J_+ := \{j \in J : y_j^M > 0\}$   
 187 ( $n_+ = 24$  in the illustrative example), but may take on the exact value  $y_j^M = 0$  at some  
 188 number  $n_- := |J_-|$  of indices  $J_- := \{j \in J : y_j^M = 0\}$  ( $n_- = 26$  in the illustrative example),

189 for a total of  $n = n_- + n_+ = |J|$  (here  $n = 50$ ) design points. Note, if the simulator output is  
 190 vector-valued, we will proceed with this imputation approach by treating each output vector  
 191 element independently. This choice is motivated by the fact that each vector element will  
 192 have its own set of design points that lead to positive outputs and to zero outputs. In other  
 193 words, each output vector element will have its own  $J_+$  and  $J_-$ . Obviously, this will add some  
 194 computational burden to the imputation, but that burden is somewhat alleviated by noting  
 195 that the imputations can be done for each element of the vector in parallel as a preprocessing  
 196 step. Through the rest of this section, we will describe the zGP imputation for scalar valued  
 197 output.

198 We construct a random field stochastic model  $\{\mathbf{x} \rightsquigarrow Z(\mathbf{x}) : \mathbf{x} \in \mathcal{X}\}$  which we view as  
 199 a joint prior distribution for the model outputs  $\{y^M\}$  at all possible input points  $\{\mathbf{x} \in \mathcal{X}\}$ ,  
 200 and then seek the posterior distribution of  $\{y^M\}$  at all locations  $\{\mathbf{x} \in \mathcal{X}\}$ , *conditional* on  $Z$   
 201 agreeing with the design,  $Z(\mathbf{x}_j) = y_j^M$  for  $j \in J$ . Because of the nonnegativity constraint we  
 202 cannot take  $\{Z(\mathbf{x})\}$  to have a multivariate Normal distribution, but we can still leverage the  
 203 vast development of Gaussian Process technology by modeling  $Z := 0 \vee \zeta$  as the maximum of  
 204 zero and a GP  $\zeta \sim \text{GP}(\mu, \Sigma)$  with some mean function  $\mu(\mathbf{x})$  and covariance function  $\Sigma(\mathbf{x}, \mathbf{x}')$  on  
 205  $\mathcal{X}$  and  $\mathcal{X}^2 = \mathcal{X} \times \mathcal{X}$ , respectively. This is the aforementioned *zero-censored Gaussian Process*,  
 206 or more succinctly, the zGP. In practice we take the mean function,  $\mu(\mathbf{x})$  to be of very simple  
 207 form— usually either a constant (possibly zero) or a linear function— and take  $\Sigma(\mathbf{x}, \mathbf{x}')$  to be  
 208 from the Matérn class with smoothness parameter  $5/2$  (see Eqn(2.1)).

209 The conditional distribution (and even the conditional mean) for  $\zeta(\mathbf{x}_i)$  at unobserved  
 210 locations in input space  $\{\mathbf{x}_i \in \mathcal{X} : i \in I\}$ , given  $Z(\mathbf{x}_j) \equiv 0 \vee \zeta(\mathbf{x}_j) = y_j^M$  for  $j \in J$ , are  
 211 unavailable in closed form. To facilitate inference we propose to draw simulations of  $\zeta(\mathbf{x}_I) :=$   
 212  $\{\zeta(\mathbf{x}_i) : i \in I\}$  of the GP  $\zeta$  at finite sets  $I$  of new input vectors  $\mathbf{x}_i$ , given  $Z(\mathcal{D}) = y^M(\mathcal{D})$ . We  
 213 can then estimate posterior expectations of  $Z(\mathbf{x}_I)$  itself or of functions of  $Z(\mathbf{x}_I)$  with ergodic  
 214 sample averages from these simulations. Even this task is challenging, since the conditional  
 215 distribution of  $\zeta(\mathbf{x}_I)$  constrained to go through non-negative output-design pairs – *i.e.*, given  
 216  $\zeta(\mathbf{x}_{J_+}) = y_{J_+}^M$  and the condition  $\{(\forall j \in J_-) \zeta(\mathbf{x}_j) \leq 0\}$  – is intractable.

217 We address this in two steps. First, we use a *substitution sampling* scheme to make  
 218 a series of imputed independent draws from the conditional distribution of  $\zeta(\mathbf{x}_{J_-})$ , given  
 219  $\zeta(\mathbf{x}_{J_+}) = Z(\mathbf{x}_{J_+})$  and the event  $\zeta(\mathbf{x}_{J_-}) \leq 0$  (*i.e.*, given  $Z(\mathbf{x}_J) = y_J^M$ ). We can then view  
 220  $\zeta(\mathbf{x}_J)$  as a fully observed draw from the  $\text{GP}(\mu, \Sigma)$  distribution, with a known  $n$ -variate Normal  
 221 distribution. For each of those imputed draws we draw  $\zeta(\mathbf{x}_I)$  from its conditional distribution  
 222 (using the usual Gaussian formulas) or, if only the mean and variance of some  $\zeta(\mathbf{x}_i)$  are of  
 223 interest, evaluate those in closed form. Algorithm 1 implements this approach. For the reader  
 224 unfamiliar with substitution sampling, we preface each step with a brief explanation in italics.  
 225 In this algorithm, we assume that the estimated GP parameter vector,  $\hat{\theta} \approx \theta$  is known. A  
 226 natural first approach is to use  $\hat{\theta}$  obtained from fitting a Gaussian process to  $(\mathbf{x}_{J_+}, y_{J_+}^M)$ . In  
 227 Section 3.3 we explore an approach to incorporate information from “nearby” zeros in esti-  
 228 mating  $\hat{\theta}$ .

229

230 **Algorithm 1: zGP substitution sampling.** To construct a zGP sample of size  $K \in \mathbb{N}$ ,  
 231 for each index  $1 \leq k \leq K$  we:

232 0) *Begin with an initial sample of output response values that are identical to positive*  
 233 *output from the simulator for inputs  $\mathbf{x}_{J_+}$  and are negative for inputs  $\mathbf{x}_{J_-}$ . A systematic*  
 234 *way to achieve this initial sample is described in Algorithm 2, but as long as the*  
 235 *constraints are met, any initial sample should work.*

236 Begin with an initial set  $\zeta^{(0)}$  at step  $t = 0$  of candidate imputed values at locations  
 237  $\mathbf{x}_J$ , with  $\zeta^{(0)}(\mathbf{x}_{J_+}) = y_{J_+}^M$  and with  $\zeta^{(0)}(\mathbf{x}_{J_-}) < 0$ .

238 1) *Select, at random, one of input design points indexed by  $J_-$ . In other words, select one*  
 239 *input design point from those that led to an output of zero. Using all of the other design*  
 240 *points except the one selected (i.e., other points indexed by  $J_-$  and all points indexed by*  
 241  *$J_+$ ), construct a GP conditioned to go through these design/response pairs, using the*  
 242 *current value of the negative imputed responses corresponding to the remaining  $\mathbf{x}_{J_-}$ .*  
 243 *Sample this GP at the selected design point from its (tractable) truncated Gaussian*  
 244 *distribution and replace its current imputed response value with this new, negative*  
 245 *sample.*

246 Select  $j^* \in J_-$  uniformly at random. Construct  $\zeta^{(t+1)}$  by setting  $\zeta^{(t+1)}(\mathbf{x}_j) = \zeta^{(t)}(\mathbf{x}_j)$   
 247 for  $j \in J_c$  where  $J_c = J \setminus j^*$  and for  $\zeta^{(t+1)}(\mathbf{x}_{j^*})$  take a random draw from the truncated  
 248 (to the negative half-line  $\mathbb{R}_-$ ) Normal distribution with mean and variance of the  
 249 conditional GP( $\mu, \Sigma$ ) distribution, given  $\{\zeta^{(t+1)}(\mathbf{x}_j) : j \neq j^*\}$ . Specifically, sample  
 250  $\zeta^{(t+1)}(\mathbf{x}_{j^*}) \sim \text{TN}(\mathbf{m}_{j^*|J_c}, \mathbf{V}_{j^*j^*|J_c})$ , where

$$(3.2) \quad \begin{aligned} \mathbf{m}_{j^*|J_c} &= \hat{\mu}(\mathbf{x}_{j^*}) + \mathbf{r}_{J_c}(\mathbf{x}_{j^*})^\top \hat{\mathbf{R}}_{J_c}^{-1} \left( \zeta^{(t+1)}(\mathbf{x}_{J_c}) - \hat{\mu}(\mathbf{x}_{J_c}) \right) \\ \mathbf{V}_{j^*j^*|J_c} &= \hat{\sigma}^2 \left( 1 - \mathbf{r}_{J_c}(\mathbf{x}_{j^*})^\top \hat{\mathbf{R}}_{J_c}^{-1} \mathbf{r}_{J_c}(\mathbf{x}_{j^*}) \right). \end{aligned}$$

251 where  $(\hat{\mathbf{R}}_{J_c})_{j,j'} = c(\mathbf{x}_j, \mathbf{x}_{j'})$  for  $j, j' \in J_c$  and the  $j$ th component of the vector  
 252  $(\mathbf{r}_{J_c}(\mathbf{x}_{j^*}))_j = c(\mathbf{x}_{j^*}, \mathbf{x}_j)$  for all  $j \in J_c$ .

253 2) *Repeat step 1 several times (a reasonable choice would be as many times as there*  
 254 *are design points leading to zero output); think of this as one pass of the substitution*  
 255 *sampler. Note, as the index sampling is random in step 1, some zero-output design*  
 256 *points may get sampled repeatedly while others may not be sampled on a given pass.*

257 Repeat step 1  $n_-$  times and increment  $t \leftarrow t + 1$ .

258 3) *Repeat passes (steps 1 and 2) to develop a sequence of of negative imputed samples*  
 259 *for  $\mathbf{x}_{J_-}$ . Note the responses corresponding tot  $\mathbf{x}_{J_+}$  will not change. Repeat until a*  
 260 *user-defined stopping criterion is reached.*

261 Repeat steps 1, 2 until a convergence criterion is met. Return  $\zeta(\mathbf{x}_J) := \zeta^{(t)}(\mathbf{x}_J)$ .

262 This generates a sequence of  $K$  iid replicates  $\zeta(\mathbf{x}_J)$  with approximately the correct GP( $\mu, \Sigma$ )  
 263 conditional distribution, consistent with the observed values of  $y_J^M$ . Now, for each of these  
 264 replicates  $\zeta(\mathbf{x}_J)$ , draw  $\zeta(\mathbf{x}_I)$  from the conditional GP( $\mu, \Sigma$ ) Gaussian distribution, given  $\zeta(\mathbf{x}_J)$ ,  
 265 and set  $Z(\mathbf{x}_I) := (0 \vee \zeta(\mathbf{x}_I))$ . If the object of interest is the posterior mean or variance of  
 266  $Z(\mathbf{x}_i)$  for some  $i \in I$ , those are available in closed form for each particular imputation of  
 267  $\zeta(\mathbf{x}_{J_-})$ .

268 We fit the zGP to our illustrative example by drawing  $N = 100$  sets of correlated imputed

269 negative samples (for  $\{\mathbf{x}_j : j \in J_-\}$ ) with a zero mean trend,  $\mu(\cdot) = 0$ . For each zero-  
 270 output design point, we took the mean value of those 100 samples, let us call these  $\{y_j^- =$   
 271  $\frac{1}{K} \sum_{k=1}^K \zeta^{(k)}(\mathbf{x}_j) : j \in J_-\}$ . Further we will let  $\mathbf{y}^{\text{Imp}} = \{y_j^- : j \in J_-\} \cup \{y_j^M : j \in J_+\}$ . Now,  
 272 we fit a GP with a linear mean trend to  $\mathcal{D}^{\text{Imp}} = \{(\mathbf{x}_j, y_j^{\text{Imp}}) : j \in J\}$ . This design, along with  
 the resulting mean surface of the GP and zGP are plotted in Fig. 3.

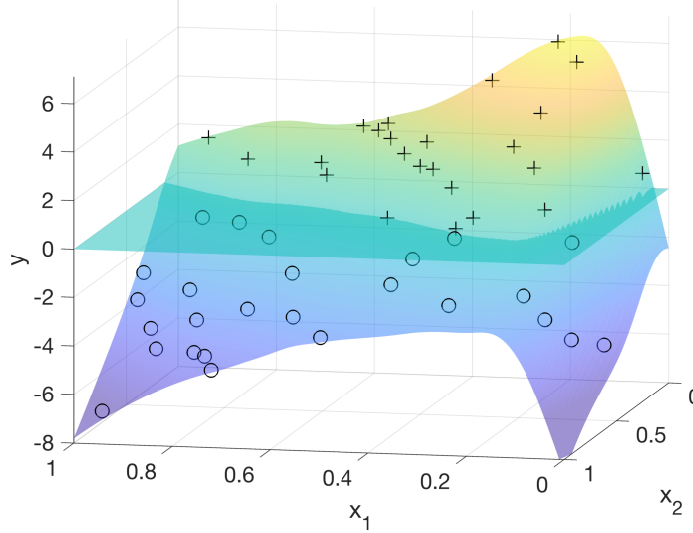


Figure 3: Mean surface of the GP fit to  $\mathcal{D}^{\text{Imp}}$  along with the maximum of that surface and zero, *i.e.*, the mean zGP. Design points from  $\mathcal{D}^{\text{Imp}}$  are also plotted with (+) corresponding to positive responses, and (o) corresponding to negative, imputed responses.

273

274

275

276

277

278

279

280

281

282

283

284

285

286

287

288

289

To further illustrate the zGP approach, and its effectiveness at modeling, we sampled the zGP (over the whole computational grid, *i.e.*, for each pixel in input/scenario space). We counted the fraction of times that the true function was zero, but the zGP provided a positive prediction. Likewise, we counted the fraction that the true function was positive, but the zGP predicted a zero. The resulting predicted false positives and false zeros yield a band of uncertainty around the true zero-contour of  $f(\cdot, \cdot)$  as can be seen in Fig. 4(a). We also repeated this illustration for smaller designs, with  $n = 50, 30,$  and  $20$ , also presented in Fig. 4. With a large number of design points, the “transition contour” from zero-predicted output to positive predicted output is very well resolved as indicated by a narrow band of predicted false zeros/false positives in Fig 4(a). The wider bands in Fig 4(b)–4(d) reflect additional uncertainty with fewer design points.

Ultimately, to fully reflect uncertainty using the zGP, one would sample the imputed replicate points  $\zeta^{(k)}(\mathbf{x}_J) = \{\zeta^{(k)}(\mathbf{x}_j) : j \in J, k = 1, \dots, K\}$  and then sample the GP conditioned on equaling  $\zeta^{(k)}(\mathbf{x}_J)$ . In practice, this may be computationally excessive. With this in mind, we explore the uncertainty in the zGP with the imputed mean,  $\mathbf{y}^{\text{Imp}}$ , by sampling that zGP. In contrast, we calculate the conditional mean of a zGP fit to each sample set of imputed

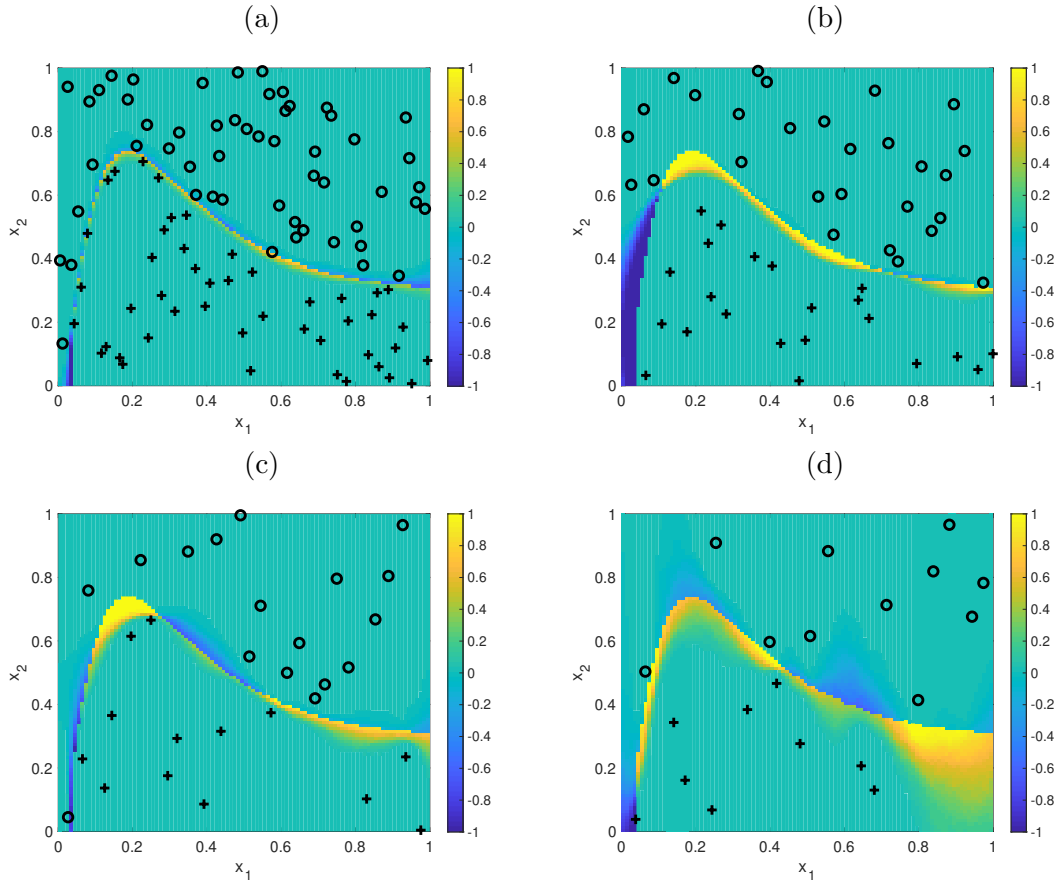


Figure 4: Fraction of samples that indicated false zero response (reported by positive values – toward yellow – on the color scale) and false positive responses (reported by negative values – toward blue – on the color scale). Number of design points,  $n$ , from Panels (a)–(d): 100, 50, 30, 20. The symbols  $\circ$  and  $+$  indicate design points that resulted in a zero response or a positive response, respectively.

290 points,  $\zeta^{(k)}(\mathbf{x}_j)$  (but we do not then sample those GPs, we only evaluate the means.) We  
 291 compare these two approximations to reflecting zGP uncertainty on the illustrative example  
 292 in Fig. 5.

### 293 3.3. Notes on fitting the zGP: initialization and range parameters.

294 **3.3.1. Initialization.** We will explore a general approach to initializing a set of negative  
 295 imputed outputs for  $\{\mathbf{x}_j : j \in J_-\}$ . This strategy is one way to obtain an initialization for  
 296 substitution sampling (step 0 in Algorithm 1). In summary, start with the set of positive  
 297 output response and corresponding design points, those indexed by  $J_+$ . We then sample a GP  
 298 fit to only these points, and evaluate that sample at all designs point indexed by  $J_-$ . If all of  
 299 these samples are negative, we are done (typically, unless the input space is one dimensional,

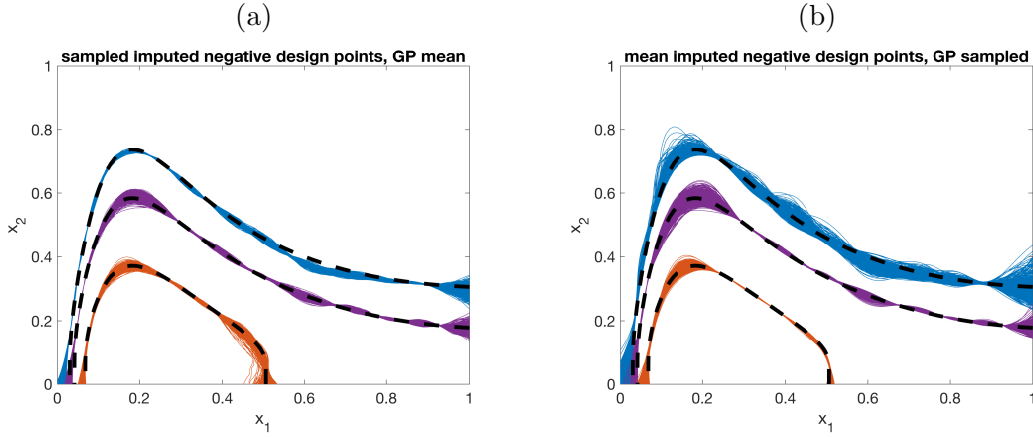


Figure 5: Panel (a): mean of imputed samples,  $\mathbf{y}^{\text{Imp}}$  is used to fit a GP with true contours at  $y = 0$ ,  $y = 1$ , and  $y = 3$ . This GP is sampled 500 times with the same contours calculated for each sample (0 is blue, 1 is purple, 3 is orange.) Panel (b): a GP fit to each of  $K = 500$  sampled sets of imputed design points,  $\zeta^{(k)}(\mathbf{x}_J)$ . The mean surface of each GP is calculated and contours plotted for each with the same color scheme indicated level.

300 this does not happen.) At this point, we collect this round of negatively sampled outputs for  
 301  $\{\mathbf{x}_j : j \in J_-\}$  along with the positive outputs, fit a GP conditioned to go through all of these  
 302 points, and then sample the GP at the remaining  $\{\mathbf{x}_j : j \in J_-\}$ . We repeat this cycle until  
 303 we have negative samples for all  $\mathbf{x}_{J_-}$ . Details of this approach follow.

304 **Algorithm 2: Initializing negative imputed samples.**

305 0) Start with a sample  $\{\zeta_j^0 : j \in J_-\} \sim \text{No}(\mathbf{m}_{J_-|J_+}, \mathbf{V}_{J_-|J_+})$ . Here we assume that  
 306  $\mu(\cdot) = 0$  and the definitions of  $\mathbf{m}$  and  $\mathbf{V}$  leading to a simpler form of Eqn 3.2:

$$(3.3) \quad \begin{aligned} \mathbf{m}_{J_-|J_+} &= \hat{\mathbf{R}}_{J_-J_+} \hat{\mathbf{R}}_{J_+J_+}^{-1} y^M(\mathbf{x}_{J_+}) \\ \mathbf{V}_{J_-J_-|J_+} &= \hat{\sigma}^2 \left( \hat{\mathbf{R}}_{J_-J_-} - \hat{\mathbf{R}}_{J_-J_+} \hat{\mathbf{R}}_{J_+J_+}^{-1} \hat{\mathbf{R}}_{J_+J_-} \right). \end{aligned}$$

307 If all  $\zeta_j^0 \leq 0$ , we are done. Otherwise set  $t = 1$ .

308 1) Set  $J_*^t = \{j \in J_- : \zeta_j^{t-1} > 0\}$  and set  $J_*^{c,t} = J \setminus J_*^t$  (not just  $J_- \setminus J_*^t$ ).

309 2) If  $J_*^t = \emptyset$ , set  $\{\zeta_j : j \in J\} = \{\zeta_j^{t-1} : j \in J_-\} \cup \{Z_j : j \in J_+\}$  and exit the loop.

310 3) Draw  $\{\zeta_j^t : j \in J_*^t\} \sim \text{No}(\mathbf{m}_{J_*^t|J_*^{c,t}}, \mathbf{V}_{J_*^t|J_*^{c,t}})$ .

311 4) Increment  $t \leftarrow t + 1$  and repeat steps 1)–4).

312 Note,  $\mathbf{m}$  and  $\mathbf{V}$  are updated in step 3) as in Eqn 3.3. Either one can utilize one sample of  
 313  $\{\zeta_j : j \in J\}$  or repeat this process  $K$  times and take the sample average for each  $j \in J$  to  
 314 initialize substitution sampling for Algorithm 1. Our illustrative example and applications  
 315 proceed with the latter.

316 **3.3.2. Fitting trend and correlation parameters..** With a negative sample for all  $j \in J_-$   
 317 in hand, before implementing the zGP substitution sampling of Algorithm 1, we select and

318 fit a mean trend for the zGP using these initial imputed points. Often a constant or a linear  
 319 trend for  $\mu(\cdot)$  is appropriate, but a particular application may benefit from a problem-specific  
 320 mean function as we will see in Section 4.

321 Until this point we have relied on fitting the GP (*i.e.*, finding reasonable range parameters)  
 322 using only the design points  $\mathcal{D}_+^M = \{(\mathbf{x}_j, y_j^M) : j \in J_+\}$  with strictly positive output  $y_j^M > 0$ .  
 323 Surely we lose some information on the range parameters by ignoring the influence of *all*  
 324 the design points that result in zero outputs. As such we propose to include a subset of  
 325 the design points that result in zero output for the purpose of fitting range parameters. We  
 326 focus our search for a prudent selection of these zeros by considering two factors: 1) the  
 327 minimum distance between each zero-output design point  $\mathbf{x}_j$  and the set of positive-output  
 328 design points, and 2) the probability of obtaining a negative sample at each zero-design point  
 329 from a GP fit to  $\mathcal{D}_+^M$ . We posit that the most influential zeros are those that are *both* close  
 330 to positive-output design points *and* have a small probability of being negative under the  
 331 original fit to  $\mathcal{D}_+^M$ . A specific choice of the number of zeros to include and/or thresholds for  
 332 each metric will be user defined. For the pedagogical example, we sorted the zero-output  
 333 design points under each metric, considered the smallest  $\frac{1}{2}n_-$  design points of each ordered  
 334 set (*i.e.*, those design points resulting in zero output that are *both* nearest to a design point  
 335 resulting in positive output *and* those that have the smallest probability of being negative  
 336 under a GP model fit only to  $\mathcal{D}_+^M$ .) Then we selected the zero-output design points in the  
 337 intersection of these two sets. This set of additional design points along with design in  $J_+$   
 338 will be indexed by  $J_+^*$ . The resulting subset is displayed in Fig. 6(a) along with all of the  
 339 design/response pairs, including the negative imputed response values,  $\mathbf{y}^{\text{imp}}$ , in Fig. 6(b). We  
 340 then compare three mode-posterior estimates of the range parameters: one set of estimates fit  
 341 to only positive outputs,  $\{(\mathbf{x}_j, \zeta_j^{(0)}) : j \in J_+\}$ ; a histogram of mode-posterior range parameter  
 342 estimates fit to positive outputs and “closest” imputed outputs,  $\{(\mathbf{x}_j, \zeta_j^{(t)}) : j \in J_+^*\}$ ; and one  
 343 set of estimates fit to positive outputs and “closest” imputed outputs,  $\{(\mathbf{x}_j, y_j^{\text{imp}}) : j \in J_+^*\}$ .  
 344 In the pedagogical example (with  $n = 50$ ) it is worth noting that dominant input variable  
 345 (*i.e.*, the one with the smallest estimated correlation length) swaps roles when fit to design  
 346 points indexed by  $J_+$  versus those indexed by  $J_+^*$ . In particular, for  $\theta_2$ , the mode estimate  
 347 found by fitting a GP to  $\mathcal{D}_+^M$  does not even fall in the support of histogram for  $\theta_2$  when  
 348 influential zero-output (and then negative imputed-output) design points are included in the  
 349 GP model. This indicates that a GP fit to only positive-output design points may not be an  
 350 optimal model for the zGP.

351 **4. Applications.** We apply the zGP to two geophysical flow applications, namely com-  
 352 puter models of storm surge from tropical storms and of volcanic flows known as pyroclastic  
 353 density currents. In each case, the inundation footprint is spatially complex and the set of  
 354 map nodes (spatial pixels on a map) that result in no-inundation (*i.e.*, zero outputs) varies  
 355 when the computer models are run at different (storm or volcanic) scenarios. We first apply  
 356 the zGP to storm surge simulations and compare the resulting zGP model to using a conven-  
 357 tion GP that does not account for the semi-binary nature of the computer model output. We  
 358 then do a more in-depth application of the zGP to pyroclastic density current simulations to  
 359 demonstrate how the zGP could be used in a probabilistic analysis of hazards.

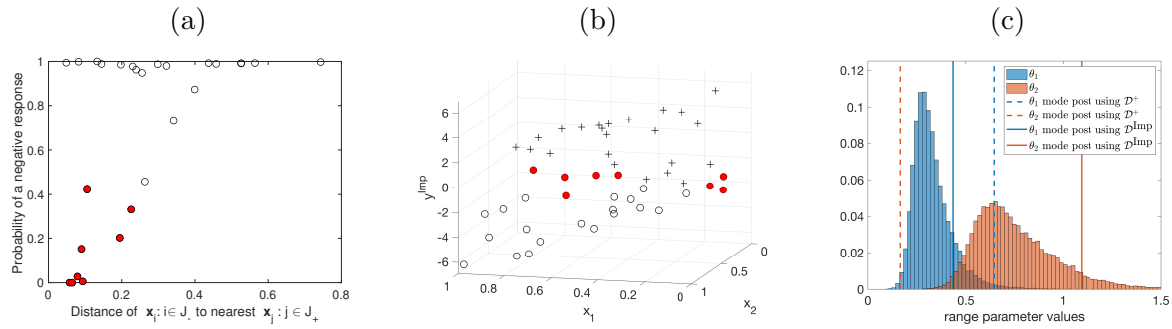


Figure 6: Pedagogical example. Panel (a): For each zero-output design point, the probability of a negative response at that input predicted by a GP model fit to only positive-output design points is plotted against the Euclidean distance (in input space) to its nearest positive-output design point. Red interiors indicate the design points that were chosen to be included in the set to fit range parameters for the zGP. Panel (b): Positive response (+) and negative imputed response (o) plotted against the corresponding design points. Again, red filled points correspond to the additional points considered to fit range parameters for the zGP. Panel (c): Mode posterior estimates of range parameters ( $\theta_1$  in blue,  $\theta_2$  in ochre). The histograms of range parameter values are those computed during the replacement sampling imputation algorithm and fit to  $\{(\mathbf{x}_j, \zeta_j^{(t)}) : j \in J_+^*\}$ . Dashed lines are fit only to  $\mathcal{D}_+^M$ . The solid lines are range parameter values fit to  $\{(\mathbf{x}_j, y_j^{\text{imp}}) : j \in J_+^*\}$ .

360 **4.1. zGP for computational models of storm surge.** Several threats are associated with  
 361 hurricanes and tropical cyclones. In addition to persistent high winds and torrential rainfall,  
 362 storm surge — flooding due to, effectively, a hurricane pushing ocean water onto land — is  
 363 often responsible for severe property damage and loss of life associated with hurricanes. In  
 364 fact, roughly half of the deaths in North America from Atlantic hurricanes in the late 20<sup>th</sup>  
 365 century/early 21<sup>st</sup> century are attributed to storm surge (Rappaport, 2014).

366 Storm surge simulators are numerically implemented models of ocean circulation that  
 367 commonly solve barotropic, depth-averaged shallow water equations over realistic bathymetry.  
 368 Such models are forced by atmospheric conditions, notably wind and atmospheric pressure,  
 369 as well as bottom drag. ADCIRC is the storm surge simulator we explore in this example  
 370 (Luettich and Westerink, 2004; Westerink et al., 2008). It employs Galerkin methods in  
 371 combination with finite elements over an unstructured mesh that is amenable to dealing with  
 372 geometrically complicated domains like coastlines.

373 The skill of storm surge simulators has increased markedly over the last few decades (Resio  
 374 and Irish, 2015), leaving the aleatory variability of storms as the major sources of uncertainty  
 375 — how big, how strong, landfalling location etc. Several recent studies apply GP-based surro-  
 376 gate methods to output from storm surge simulations that vary storm parameterizations as  
 377 inputs (Jia and Taflanidis, 2013; Jia et al., 2016; Zhang et al., 2018; Yang et al., 2019; Taflan-  
 378 idis et al., 2020; Plumlee et al., 2021). Some studies ignore the zero-problem by focusing on  
 379 “all wet” map nodes while others use an ad-hoc spatial interpolation for imputing replace-

380 ment values for zeros. Here we apply a principled, model-based approach to imputation that  
 381 can be used in conjunction with ad-hoc approaches, or to replace imputation for problematic  
 382 map nodes, or when detailed spatial information is not available. In this study we focus on  
 383 storms that threaten southwest Florida, USA. We consider a latin hypercube design of 200  
 384 storms. These are parameterized at landfall by: latitude of the storm's center, a storm's central  
 385 pressure deficit ( $dp$  – indicates a storm's intensity), radius of maximum wind speed ( $r_{mw}$   
 386 – indicates a storm's size), storm forward speed ( $v_f$ ), storm heading ( $\theta$  – angle of incidence,  
 387 measured in degrees clockwise from 0 at due North), and Holland's  $B$  (a shape parameter to  
 388 the radial wind and pressure fields).

389 The design for this study along with a grid of 908 map nodes where simulated max storm  
 surge output is recorded are shown in Fig. 7. In this simulated storm surge data set, 559 of

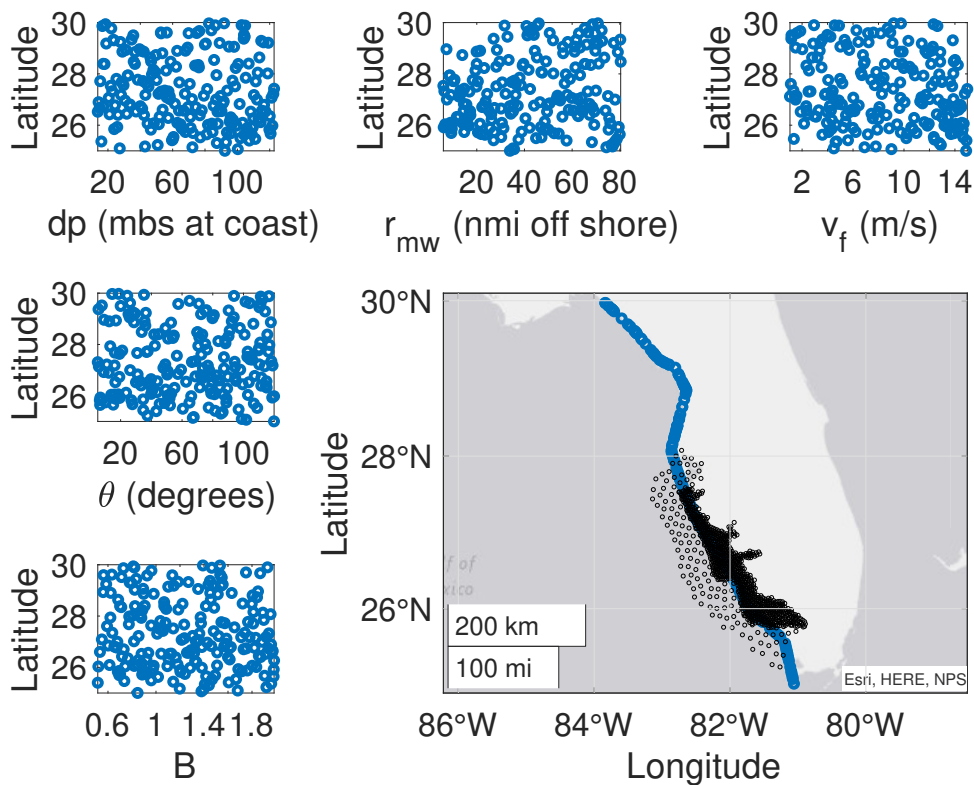


Figure 7: Storm surge simulator design. The lower right plot shows the landfall location of 200 simulated storms (blue circles) along with an unstructured grid of map nodes under consideration for storm surge inundation. Each of the scatter plots is Latitude of the storm's center at landfall vs one of the other storm parameters at landfall, clockwise from lower left: Holland's  $B$ , angle of incidence, central pressure deficit (millibars), radius of maximum wind speed (nautical miles), and forward speed.

the 908 map nodes have some “dry” storms (zeros recorded as output at that node) ranging from one dry storm to 193 dry storms of the 200 simulated storms. We fit the zGP to the storm surge output for each of 559 nodes and impute negative values to replace the zero-valued outputs. Then we apply PCA to the full data set of storm surge inundation and negative imputed storm surges to perform dimension reduction on over the 908 spatial modes. Keeping 10 PCA modes, we then fit GPs to each of the 10 associated PCA loadings as output with the input design described in Fig. 7. Then we construct predicted surges by computing loadings given by the GP predictive mean evaluated at the left-out storm parameter inputs. Finally, we take the predicted surge at each node to be the maximum of that given by the GP+PCA reconstruction and zero.

To demonstrate the efficacy of the zGP in this case, we perform leave-out experiments and predict storm surge inundation depths for cases not used to fit the emulator. In Fig. 8 we leave out four representative storms, and use the zGP emulator as just described to estimate the output of the four left-out ADCIRC storm surge simulations. We also show the signed differences which, for the storms under consideration, range  $\pm 1$  meter. We also consider a full leave-one-out experiment and calculate predicted errors for each storm at each node ( $200 \times 908 = 161,800$  errors.) For comparison, we build two PCA-based emulators – one on the original data set including all of the zeros, and one on the zGP imputed negatives-for-zeros data set. Fig. 9 shows normalized histograms of error magnitudes for each of these two cases. The zGP-imputed error histogram has more mass for small errors (say,  $\leq 0.2\text{m}$ ) which one might anticipate as the imputation adds information for storms that are “near misses” vs “far off.” We also found that the zGP has many fewer large errors (say  $\geq 2\text{m}$ ) which is a somewhat surprising result.

**4.2. zGP for volcanic hazard analysis.** Pyroclastic density currents (PDCs) are hot, fast-moving flows made of gas and volcanic particles of very different sizes (Sulpizio et al., 2014). Their destructive potential is extremely high and they have caused the greatest number of fatalities related to volcanic activity over the last centuries (Brown et al., 2017). PDC generation mechanisms and initial conditions, including the spatial location of the eruptive vent, are quite complex and can vary significantly from one eruption to another, or even within a single eruptive episode. Additionally, understanding and hence forecasting the spatio-temporal propagation of PDCs, which is largely influenced by the topography at a given volcanic system, stands as an arduous challenge in modern volcanology (*e.g.*, Dufek (2016)). PDC initiation can either be modeled as one or more piles of material that collapse under their own weight, or one or more fluxes of material that collapse back to the ground after losing their vertical momentum (*e.g.*, Charbonnier and Gertisser (2012); Esposti Ongaro et al. (2007); Valentine and Sweeney (2018)). The flows then propagate under the action of gravity and lose momentum due to frictional forces acting both within the flow and at the interface between the flow and the basal surface (Pitman et al. (2003); Patra et al. (2005); see also [https://vhub.org/resources/4057/download/Titan2D\\_User\\_Guide.pdf](https://vhub.org/resources/4057/download/Titan2D_User_Guide.pdf)).

In order to quantify aleatory and epistemic uncertainties related to PDC generation and propagation, and therefore fully quantify a PDC hazard, several modeling strategies have been recently adopted (Dalbey et al., 2008; Neri et al., 2015; Sandri et al., 2018; Tierz et al., 2018). One such strategy is to build GP emulators of the computer model outputs from the widely

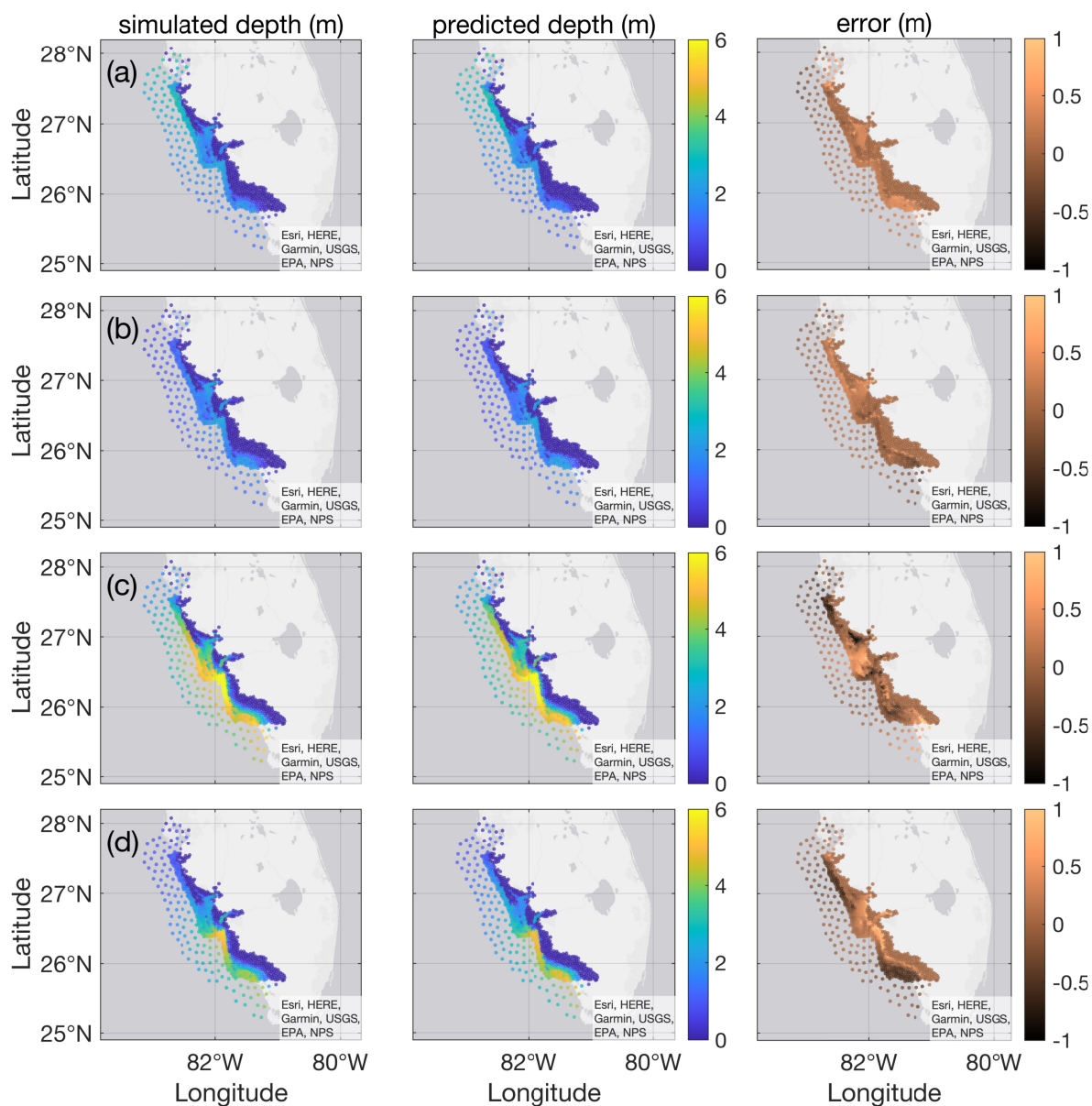


Figure 8: Left column: storm surge depths from four simulated storms labeled (a)–(d) (note these are the same simulated storms as in Fig. 1.) For visualization purposes, the surge depth color scale is set from 0 to 6m although a few nodes exceed surge depths of 6m for storms labeled c and d. Middle column: estimated storm surge depth utilizing emulators with zGP imputation for the parameterized storms (a)–(d). Right column: signed error in storm surge estimation defined as the difference between simulation depth and estimated depth at each node. Note here that the color scale varies from -1m to 1m.

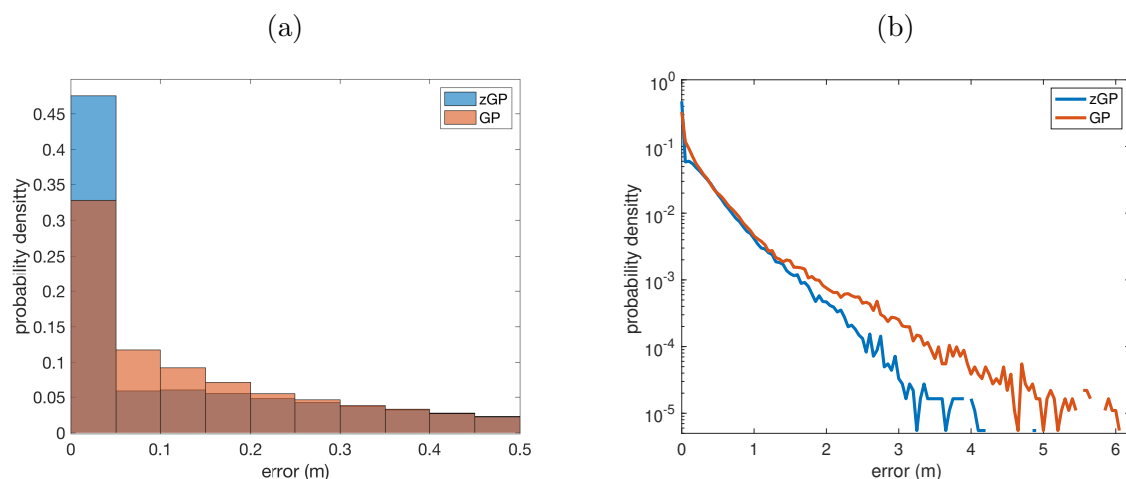


Figure 9: Normalized histograms of the magnitude error between simulated and emulated storm surge depths. Blue corresponds to emulators fit with zGP imputed values for zeros while ochre corresponds to emulators fit to output including zeros. Panel (a): Truncated histogram to compare the mass of the two cases for small amplitude errors. Panel (b): Histograms heights plotted on a logarithmic scale against error in order to visualize the relative frequency of large predicted storm surge errors for the two emulators.

434 used and freely available software TITAN2D (Patra et al., 2005). TITAN2D offers numerical  
 435 approximations to a hyperbolic system of PDEs, solved over a digital elevation model (DEM),  
 436 for modeling dry granular flows as “shallow-water” along with constitutive friction terms to  
 437 account for the granular nature of the flowing mass. The TITAN2D-GP strategy to quantify  
 438 PDC hazards has been successfully implemented at a few volcanic systems (Bayarri et al.,  
 439 2015; Rutarindwa et al., 2019; Spiller et al., 2020), but with the zero-censoring handled in  
 440 an ad-hoc manner. In this manuscript, we illustrate how the zGP emulator can be used in  
 441 conjunction with TITAN2D, and applied to probabilistic volcanic hazard assessment of PDCs.

442 We choose Aluto volcano, in central Ethiopia, as an illustrative volcanological example of  
 443 hazard analysis utilizing the zGP emulator for three reasons: (1) like other volcanic systems  
 444 worldwide (Connor and Hill, 1995; Selva et al., 2012; Bebbington, 2012), Aluto has shown sig-  
 445 nificant spatial variability in the location of its eruptive vents (Hutchison et al., 2014; Clarke  
 446 et al., 2020); (2) evidence from geological fieldwork from the most recent eruptive period at  
 447 Aluto suggests that new PDCs may be relatively small in volume (Clarke, 2020); and (3)  
 448 the topography at Aluto volcano (Fig. 1-left) is more complicated than many other volcanoes  
 449 (Branney and Acocella, 2015; Davidson and de Silva, 2000; Grosse et al., 2009; Clarke et al.,  
 450 2020). The combination of factors (2) and (3) above implies that many of the (real and simu-  
 451 lated) PDC events at Aluto are expected to result in complex, but relatively small inundation  
 452 footprints across the hazard domain. In other words, many points of interest will not be in-  
 453 undated by typical PDCs and hence TITAN2D output there will present GP emulation with  
 454 the “zero problem”. Hence, Aluto volcano represents an interesting volcanological example

TITAN2D parameter	minimum value	maximum value
$x_1$ : Flux-source (vent) radius, $r$ [m]	1.0	148.3
$x_2$ : Flux rate, $h$ [m/s]	20.0	148.4
$x_3$ : Bed friction angle [deg]	6.1	26.8
$x_4$ : Vent location, UTM Easting [m]	475260	480930
$x_5$ : Vent location, UTM Northing [m]	855190	862860
(fixed parameters)		value
Internal friction angle [deg]		30.0
Flux-source duration, ( $d$ ) [s]		240
Stopping time [s]		400
(calculated quantity: $v_{\text{PDC}} = \pi x_1^2 x_2 d / 4$ )	minimum value	maximum value
PDC volume [M m <sup>3</sup> ]	0.053	500

Table 1: TITAN2D parameter values under consideration in this illustrative study of PDC hazard analysis at Aluto volcano (Ethiopia.)

455 for the use of zGP emulators for probabilistic hazard quantification.

456 We are aiming to model column-collapse PDCs (Sulpizio et al., 2014) with TITAN2D, so  
457 we adopt a different and more realistic approach to scenario modeling (*e.g.*, the choice the  
458 input/scenario space for our simulation design that more closely mimics the physical initiation  
459 processes) than taken in previous approaches (Tierz et al., 2018; Rutarindwa et al., 2019). In  
460 total, we explore five uncertain TITAN2D inputs: vent radius, influx rate, bed friction angle,  
461 and Easting and Northing Universal Transverse Mercator (UTM) coordinates of the vent  
462 location. In terms of vent locations, vents could open over a large area (about 300 km<sup>2</sup>)  
463 across the volcanic edifice of Aluto and its surroundings. Here, we illustrate our results by  
464 focusing on two nearby map points located on the SE area of the volcano (Fig. 1-left). The  
465 area covered by the TITAN2D simulations that are relevant to potential inundation at those  
466 map points is approximately 30 km<sup>2</sup>. That is, given the parameter ranges we are considering,  
467 no PDCs are able to inundate the locations of interest if they initiate from a vent location  
468 outside this 30 km<sup>2</sup> zone. For each map location, we use a subdesign of 250 simulations,  
469 which is a subsample of a Latin hypercube design that covers the entire hazard domain. The  
470 subdesign points are chosen to include all runs that lead to inundation at the location of  
471 interest along with the simulations resulting in zero output that are nearest in design space  
472 to scenarios leading to inundation (as in Rutarindwa et al. (2019).) The subdesign along with  
473 indication of resulting inundation (or not) at one or both locations of interest is shown below  
474 in Fig. 12 and ranges of input design values are given in Table 1.

475 To demonstrate the efficacy of the zGP for analyzing inundation hazards of PDCs at  
476 Aluto, we compare the predictive mean of the zGP to that of a GP fit only to design points  
477 resulting in positive flows, and to a GP that expands on that set to include selected zero-  
478 output design points as in Spiller et al. (2014). It is clear that the zGP can readily define  
479 the boundary between inundation and no inundation while the GPs that ignore most or all of  
480 the zero-outputs struggle to do so. Figure 11-a is particularly revealing of the benefits of the

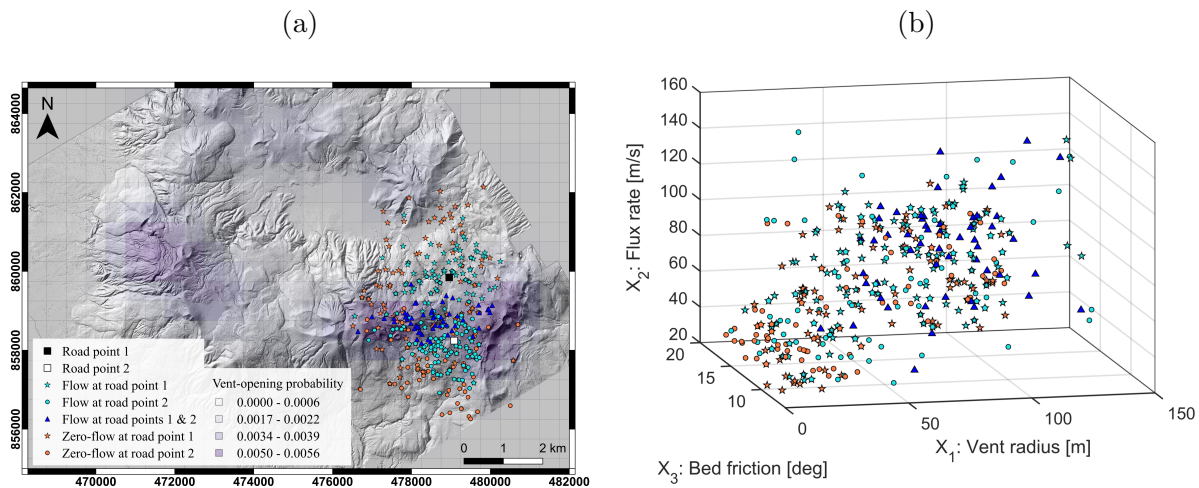


Figure 10: Summary of TITAN2D input subdesign points and corresponding outputs used to build zGP emulators for quantifying hazard probabilities at two locations of interest (road points) at Aluto volcano, Ethiopia (see simplified geographical context in the top-left corner of Fig. 1-left.) Panel (a): Spatial vent locations subdesign points plotted on a base map that is a 2-meter-resolution LiDAR Digital Elevation Model (DEM) (Hutchison et al., 2014). For reference, the vent opening probability density function from (Clarke et al., 2020) is shaded in purple with darker shades representing higher probability. Likewise, the two map points of interest (road points) are plotted along with all of the subdesign vent locations. Note, the symbols to mark these points also reflect if the resulting TITAN2D simulation inundated one or both point road points, and whether it is included as a zero in the design data set for that road point. Panel (b): a 3-D scatter plot of the other design variables (vent radius, flux rate and bed friction) marked with symbols corresponding to the vent location design and legend in Panel (a).

481 zGP. The zGP transition to zero follows the intuitive boundary of the caldera rim, *i.e.*, flows  
 482 originating at vents outside of the caldera rim (except those just to the south), will not result  
 483 inundation at road point 1, and only the zGP captures that behavior. Further, figure 11-a  
 484 demonstrates a “rebound” of the GP mean predictions back to positive inundation in regions  
 485 where no flow simulations result in inundation (see top panel in figure 11-a, toward the north  
 486 side of caldera rim.) As the zGP includes all of those zero-outputs, it does not suffer such  
 487 issues which would be highly problematic if used in a hazard analysis.

488 To perform the hazard analysis, we build a zGP emulator  $\tilde{y}$  using TITAN2D output at  
 489 each of the map points of interest (indexed by  $k$ ) to approximate the maximum PDC flow  
 490 height  $\tilde{y}_k(\mathbf{x}) \approx y_k(\mathbf{x})$  where  $\mathbf{x} = [\text{vent radius, flux rate, bed friction angle, UTM Easting, UTM}$   
 491  $\text{Northing}]$ . We define the hazard scenario domain  $\mathcal{D}$  to be the five dimensional hypercube with  
 492 vertices in each of the  $j$  dimensions varying from  $\min(x_j)$  to  $\max(x_j)$  with those values given  
 493 in Table 1. We further define PDC inundation to be a maximum inundation height,  $y_k$ , of at

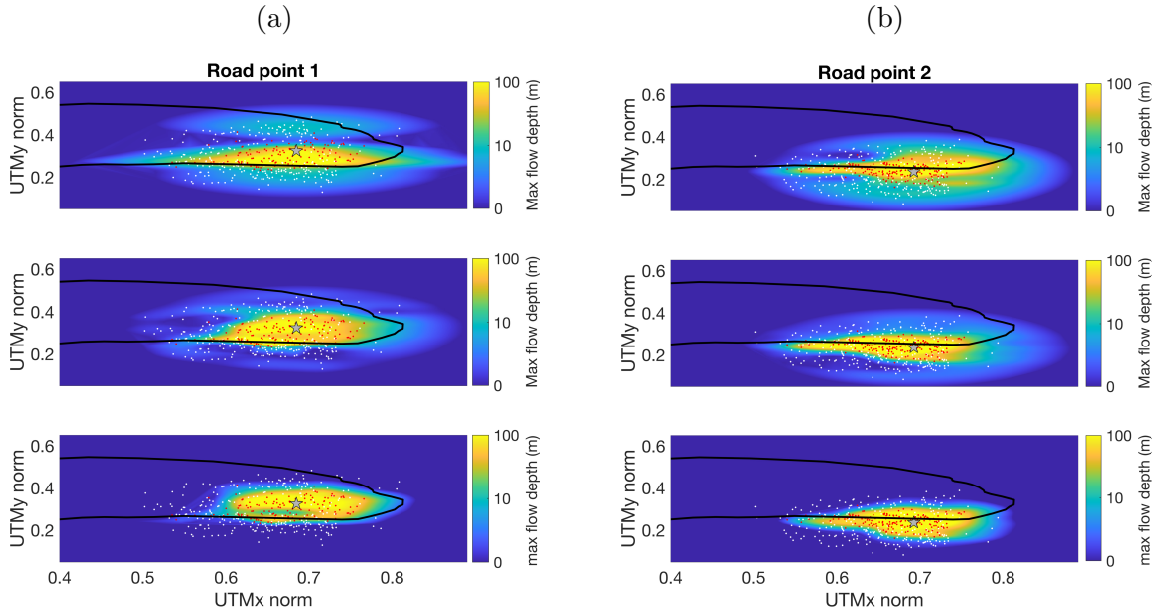


Figure 11: Panel (a): Emulator mean evaluations at road point 1. Panel (b): Emulator mean evaluations at road point 2. For each figure, UTMx and UTMy coordinates of the design points are plotted in red if flows originating at those coordinates led to positive inundation at the respective road point (labeled with a star), and in white if they led to no inundation. A black contour representing the caldera rim is plotted in each figure for reference. Blue-yellow pixels in each figure represents the mean of a GP prediction evaluated at each (UTMx, UTMy) coordinate for a fixed volume and basal friction (with color applied on a log scale in meters.) Top row: mean evaluations of a GP fit only to design points with positive (red) output. Middle row: same as top row with a few additional design points with zero-output. Bottom row: zGP fit to all design points.

494 least  $h_{\text{crit}} = 0.1\text{m}$ , and define the probability of inundation for location  $k$  as

$$(4.1) \quad P_k(\text{inundation} \mid \text{PCD occurs}) = \int_{\mathcal{D}} \mathbf{1}_{\{y_k(\mathbf{x}) \geq h_{\text{crit}}\}} p(\mathbf{x}) d\mathbf{x}$$

$$(4.2) \quad \approx \frac{1}{M} \sum_{i=1}^M \mathbf{1}_{\{\tilde{y}_k(\mathbf{X}_i) \geq h_{\text{crit}}\}}, \quad \mathbf{X}_i \sim p,$$

495 where  $p(\cdot)$  is the probability density function describing the aleatory variability of potential  
 496 hazard scenarios and  $\mathbf{1}_{\{\text{Event}\}}$  is an indicator function that takes on one if the event happens  
 497 and zero otherwise. In our MC computations, we take  $M = 10^5$  replicates. To explore the  
 498 effects of aleatory uncertainty on vent opening, we compare two vent opening models over  
 499 a  $100 \text{ km}^2$  region encompassing the hazard domain:  $p(x_4, x_5)$  as uniform, and  $p(x_4, x_5)$  as  
 500 the vent opening model developed by Clarke et al. (2020). In our exploration we fix the bed

501 friction at  $15^\circ$ , *i.e.*, set  $p(x_3) = \delta(x - 15)$ . Vent radius and flux are treated differently in each  
502 of our two analyses as described below.

503 To compute the results displayed in Fig. 12-a, we assume the vent radius and flux are  
504 distributed uniformly from across their respective domains. For each sample of  $p(\mathbf{x})$ , we  
505 calculate the resulting volume  $V_{\text{PDC}} = \pi X_1^2 X_2 d$ , and compute the estimated probability of  
506 inundation as function of the PDC volume,  $v_{\text{PDC}}$ . Additionally, we sample both vent opening  
507 models as described above over the vent-opening domain shown in Fig. 12-b as a red outlined  
508 rectangle. Our assumption is that this domain covers all vent locations that can – in a  
509 volcanologically plausible sense – result in PDC inundation at map points of interest. This  
510 choice is both consistent with the results presented here (Fig. 1-left) as well as estimates of  
511 maximum flow runout from our exploratory study of TITAN2D simulations at Aluto. From  
512 this hazard analysis we see that the probability of inundation at both road points assuming  
513 the Clarke model of vent opening is roughly double that of assuming a uniform model of  
514 vent opening. Interestingly under the uniform model, the probability of PDC inundation for  
515 road point two is less than the probability of inundation at road point one, but under the  
516 Clarke model the probability of inundation at road point two is greater than at road point  
517 one. Use of the zGP in such hazard analysis enables this kind of rapid comparison of uncertain  
518 modeling assumptions. In Fig. 12-b, the values of conditional probability of PDC inundation  
519 obtained by building zGP emulators on each of a grid of map points over a small hazard  
520 domain ( $\sim 4 \text{ km}^2$  in area). In this calculation, the volume is fixed at  $\approx 0.01 \text{ km}^3$  by taking  
521  $p(x_1)p(x_2) = \delta(x_1 - 30)\delta(x_2 - 60)$  (*i.e.*, the emulator is evaluated at  $x_1 = 30$ , and  $x_2 = 60$ )  
522 and the Clarke vent opening distribution is sampled. The latter analysis serves to illustrate  
523 how our approach could be expanded to a full probabilistic volcanic hazard assessment via  
524 construction of probabilistic hazard maps (Clarke et al., 2020; Spiller et al., 2014, 2020; Tierz  
525 et al., 2018, 2020; Rutarindwa et al., 2019).

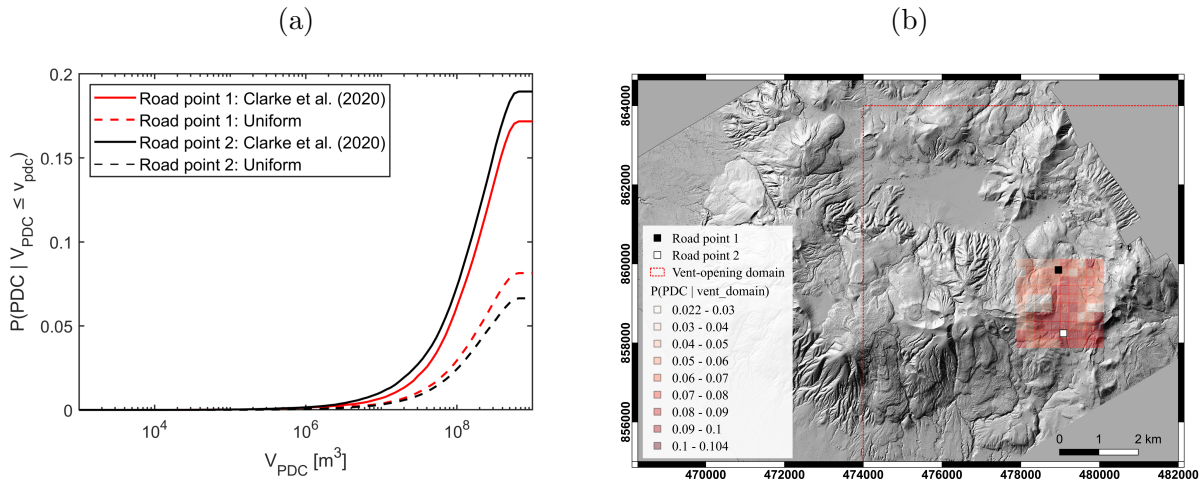


Figure 12: Summary of the illustrative probabilistic hazard analysis utilizing the zGP for example locations at Aluto volcano, Ethiopia. Panel (a): Conditional probability of PDC inundation (given PDC volume) at road points 1 and 2, for different PDC volume thresholds, calculated by Monte Carlo evaluation of the zGP emulators fitted at these points (see text for more details). Two different hazard models in terms of the aleatory variability in vent opening are explored: the model presented in (Clarke et al., 2020) and an equal (*i.e.*, Uniform)-vent-opening-probability model. Panel (b): Conditional probability of PDC inundation (given vent locations within a given spatial domain: red dashed line) over a hazard grid composed of 100 points, covering an area of approximately 4 km<sup>2</sup>, calculated by Monte Carlo evaluation of the zGP emulators fitted at these map points (see text for more details). Road points 1 and 2 are shown for reference in Fig. 1 as well.

526 **5. Discussion and conclusions.** In this work, we have introduced a zero-censored Gauss-  
 527 ian process as a systematic, model-based approach to apply GPs to range-constrained simu-  
 528 lator output. This approach relies on imputing replacement computer model runs resulting  
 529 in zero output (or, attaining the max/min of a range constraint) that intentionally violate  
 530 the constraint of non-negativity. Then a GP is constructed utilizing the negative imputed  
 531 data in place of zero-output data, and zGP predictions at untested inputs are taken to be the  
 532 maximum of the GP and zero. Moreover, the zGP can be applied as a pre-processing step to  
 533 then be used in conjunction with other GP advances. In Section 4 we applied the zGP before  
 534 implementing two common approaches to handling large-dimensional output data, namely the  
 535 parallel-partial emulator and GPs on PCA loadings.

536 The zGP approach overcomes several challenges associated with range-constrained output.  
 537 By construction, the GP utilized in the zGP has full support. The imputed data also allows  
 538 us to avoid the (nearly ubiquitous) non-stationarity that arises in models fit directly to range  
 539 constrained model output – flat over some regions of input space and varying over others.  
 540 This non-stationarity offers a particular challenge for vector-valued output (*e.g.*, storm surge  
 541 and PDC models) as the sets of design points that result in zero outputs change as we consider

542 different components of the vector-valued output (*e.g.*, different map nodes in geophysical flows  
 543 have different inputs in the design that lead to no flow.) This issue is a formidable challenge for  
 544 approaches that partition the input space and utilize different kernels on different partitions to  
 545 handle non-stationarity. Further, the transition of the computer model output from positive  
 546 values to zero may not be smooth, and most likely will not occur exactly at design points.  
 547 The zGP can readily estimate these transitions without assumptions on the geometry of the  
 548 input space. Lastly, there is some computational overhead in fitting a zGP for vector-valued  
 549 outputs, but those computations are a “distributable” preprocessing step.

550 We applied the zGP to a pedagogical example, and to two geophysical flow examples.  
 551 Yet, like many new methodologies, the potential of the zGP lies in ease of implementation  
 552 and wide applicability. For storm surge hazard analysis, the zGP may prove useful for map  
 553 nodes (subsets of the vector-valued output) where imputation based on topographic inter-  
 554 polation (Kyprioti et al., 2021) is unsuccessful. It will likely prove quite useful for spatial  
 555 processes with nearly no topographic influences, or those that do not have “easily modeled”  
 556 topographic influences. For example, an interesting application of the zGP is a systematic  
 557 study to understand the influence topography on pyroclastic flows where the topography has  
 558 complex features (*e.g.*, more in depth studies on volcanoes like Aluto which was examined in  
 559 Section 4.) Spatially-varying dynamic infectious disease models offer another example where  
 560 the zGP may prove a powerful tool for validation and uncertainty quantification. Of course,  
 561 there are a wide array of vector-valued outputs without spatial dependence – lengths, vol-  
 562 umes, etc – that must be positive or bounded, and the zGP has the potential to enable GP  
 563 surrogate modeling for such problems. Additionally, one could imagine using the zGP in con-  
 564 junction with derivative constrained GP construction as in (Wang and Berger, 2016) to meet  
 565 monotonicity constraints.

566 **Acknowledgements.** We would like to acknowledge support for ETS from NSF-DMS  
 567 2053872, 1821338; for RLW from NSF-DMS 1821289. We would like to thank Ben Clarke,  
 568 Eliza Calder, Bruce Pitman, Sarah Ogburn, Firawalin Dessalegn, Gezahegn Yirgu, Pierre  
 569 Barbillon, Susan Loughlin and Luigi Passarelli for useful discussions.

## 570 **References.**

- 571 P. Abrahamsen and F. E. Benth. Kriging with inequality constraints. *Mathematical Geology*,  
 572 33(6):719–744, 2001. doi: 10.1198/TECH.2009.08019.
- 573 C. Agrell. Gaussian processes with linear operator inequality constraints. *Journal of Machine*  
 574 *Learning Research*, 20(135):1–36, 2019. URL <http://jmlr.org/papers/v20/19-065.html>.
- 575 L. S. Bastos and A. O’Hagan. Diagnostics for Gaussian process emulators. *Technometrics*, 51  
 576 (4):425–438, 2009. doi: 10.1198/TECH.2009.08019.
- 577 M. J. Bayarri, J. O. Berger, E. S. Calder, K. Dalbey, S. Lunagómez, A. K. Patra, E. B.  
 578 Pitman, E. Spiller, and R. L. Wolpert. Using statistical and computer models to quantify  
 579 volcanic hazards. *Technometrics*, 51(4):402–413, 2009. doi: 10.1198/TECH.2009.08018.
- 580 M. J. Bayarri, J. O. Berger, E. S. Calder, A. K. Patra, E. B. Pitman, E. T. Spiller, and R. L.  
 581 Wolpert. A methodology for quantifying volcanic hazards. *International Journal of Un-*  
 582 *certainty Quantification*, 5(4):297–325, 2015. doi: 10.1615/Int.J.UncertaintyQuantification.  
 583 2015011451.

- 584 M. S. Bebbington. Models for temporal volcanic hazard. *Statistics in Volcanology*, 1:1–24,  
585 2012. doi: 10.5038/2163-338X.1.1.
- 586 J. Beck and S. Guillas. Sequential design with mutual information for computer experiments  
587 (MICE): Emulation of a tsunami model. *SIAM/ASA Journal of Uncertainty Quantification*,  
588 4(1):739–766, 2016. doi: 10.1137/140989613.
- 589 M. Ben Salem, F. Bachoc, O. Roustant, F. Gamboa, and L. Tomaso. Gaussian process-based  
590 dimension reduction for goal-oriented sequential design. *SIAM/ASA Journal of Uncertainty*  
591 *Quantification*, 7(4):1369–1397, 2019. doi: 10.1137/18M1167930.
- 592 M. Branney and V. Acocella. Calderas. In H. Sigurdsson, B. Houghton, S. R. McNutt,  
593 H. Rymer, and J. Stix, editors, *The Encyclopedia of Volcanoes*, chapter 16, pages 299–315.  
594 Elsevier, second edition, 2015. doi: 10.1016/B978-0-12-385938-9.00016-X.
- 595 S. K. Brown, S. F. Jenkins, R. S. J. Sparks, H. Odbert, and M. R. Auker. Volcanic fatalities  
596 database: analysis of volcanic threat with distance and victim classification. *Journal of*  
597 *Applied Volcanology*, 6(1):1–20, 2017. doi: 10.1186/s13617-017-0067-4.
- 598 S. J. Charbonnier and R. Gertisser. Evaluation of geophysical mass flow models using the  
599 2006 block-and-ash flows of Merapi Volcano, Java, Indonesia: Towards a short-term hazard  
600 assessment tool. *Journal of Volcanology and Geothermal Research*, 231:87–108, 2012. doi:  
601 10.1016/j.jvolgeores.2012.02.015.
- 602 B. A. Clarke. *Post-caldera eruptions and pyroclastic density current hazard in the Main*  
603 *Ethiopian Rift*. PhD thesis, University of Edinburgh, 2020.
- 604 B. A. Clarke, P. Tierz, E. Calder, and G. Yirgu. Probabilistic volcanic hazard assessment  
605 for pyroclastic density currents from pumice cone eruptions at Aluto volcano, Ethiopia.  
606 *Frontiers in Earth Science: Geohazards and Georisks*, 8, 2020. doi: 10.3389/feart.2020.  
607 00348.
- 608 C. B. Connor and B. E. Hill. Three nonhomogeneous Poisson models for the probability of  
609 basaltic volcanism: application to the Yucca Mountain region, Nevada. *Journal of Geo-*  
610 *physical Research: Solid Earth*, 100(B6):10107–10125, 1995. doi: 10.1029/95JB01055.
- 611 C. Currin, T. Mitchell, M. Morris, and D. Ylvisaker. A Bayesian approach to the design and  
612 analysis of computer experiments. Technical report, Oak Ridge National Laboratory, Oak  
613 Ridge, TN (USA), 1988. URL <https://www.osti.gov/biblio/6734087>.
- 614 S. Da Veiga and A. Marrel. Gaussian process modeling with inequality constraints. *Annales*  
615 *de la Faculté des sciences de Toulouse: Mathématiques*, Série 6, 21(3):529–555, 2012. doi:  
616 10.5802/afst.1344.
- 617 S. Da Veiga and A. Marrel. Gaussian process regression with linear inequality constraints.  
618 *Reliability Engineering & System Safety*, 195:1–13, 2020. doi: 10.1016/j.res.2019.106732.
- 619 K. Dalbey, A. . Patra, E. B. Pitman, M. I. Bursik, and M. F. Sheridan. Input uncertainty  
620 propagation methods and hazard mapping of geophysical mass flows. *Journal of Geophysical*  
621 *Research: Solid Earth*, 113(B5):1–16, 2008. doi: 10.1029/2006JB004471.
- 622 J. Davidson and S. de Silva. Composite volcanoes. In H. Sigurdsson, B. Houghton, S. R.  
623 McNutt, H. Rymer, and J. Stix, editors, *The Encyclopedia of Volcanoes*, chapter 43, pages  
624 663–681. Academic Press, San Diego, CA, first edition, 2000. URL <https://booksite.elsevier.com/9780126431407/netscape4/pdfs/CH43.pdf>.
- 625 J. Dufek. The fluid mechanics of pyroclastic density currents. *Annual Review of Fluid Me-*  
626 *chanics*, 48:459–485, 2016. doi: 10.1146/annurev-fluid-122414-034252.

- 628 T. Esposti Ongaro, C. Cavazzoni, G. Erbacher, A. Neri, and M.-V. Salvetti. A parallel multi-  
629 phase flow code for the 3D simulation of explosive volcanic eruptions. *Parallel Computing*,  
630 33(7-8):541–560, 2007. doi: 10.1016/j.parco.2007.04.003.
- 631 R. B. Gramacy and H. K. H. Lee. Bayesian treed Gaussian process models with an application  
632 to computer modeling. *Journal of the American Statistical Association*, 103(483):1119–1130,  
633 2008. doi: 10.1198/016214508000000689.
- 634 P. Grosse, B. van Wyk de Vries, I. A. Petrinovic, P. A. Euillades, and G. E. Alvarado.  
635 Morphometry and evolution of arc volcanoes. *Geology*, 37(7):651–654, 2009. doi: 10.1130/  
636 G25734A.1.
- 637 M. Gu and J. O. Berger. Parallel partial Gaussian process emulation for computer models  
638 with massive output. *The Annals of Applied Statistics*, 10(3):1317–1347, 2016. doi: 10.  
639 1214/16-AOAS934.
- 640 D. Higdon, J. Gattiker, B. Williams, and M. Rightley. Computer model calibration using  
641 high-dimensional output. *Journal of the American Statistical Association*, 103(482):570–  
642 583, 2008. doi: 10.1198/016214507000000888.
- 643 W. Hutchison, D. M. Pyle, T. A. Mather, J. Biggs, and G. Yirgu. *2012 Aluto LiDAR data*,  
644 2014.
- 645 G. Jia and A. A. Taflanidis. Kriging metamodeling for approximation of high-dimensional wave  
646 and surge responses in real-time storm/hurricane risk assessment. *Computer Methods in*  
647 *Applied Mechanics and Engineering*, 261–262:24–38, 2013. doi: 10.1016/j.cma.2013.03.012.
- 648 G. Jia, A. A. Taflanidis, N. C. Nadal-Caraballo, J. A. Melby, A. B. Kennedy, and J. M.  
649 Smith. Surrogate modeling for peak or time-dependent storm surge prediction over an  
650 extended coastal region using an existing database of synthetic storms. *Natural Hazards*,  
651 81(2):909–938, 2016. doi: 10.1007/s11069-015-2111-1.
- 652 A. P. Kyprioti, A. A. Taflanidis, M. Plumlee, T. G. Asher, E. T. Spiller, R. A. Luettich,  
653 B. Blanton, T. L. Kijewski-Correa, A. Kennedy, and L. Schmied. Improvements in storm  
654 surge surrogate modeling for synthetic storm parameterization, node condition classification  
655 and implementation to small size databases. *Natural Hazards*, 109(2):1349–1386, 2021. doi:  
656 10.1007/s11069-021-04881-9.
- 657 K. Kzyurova. *On Uncertainty Quantification for Systems of Computer Models*. PhD thesis,  
658 Duke University, 2017.
- 659 X. Liu and S. Guillas. Dimension reduction for Gaussian process emulation: An application  
660 to the influence of bathymetry on tsunami heights. *SIAM/ASA Journal of Uncertainty*  
661 *Quantification*, 5(1):787–812, 2017. doi: 10.1137/16M1090648.
- 662 A. F. López-Lopera, F. Bachoc, N. Durrande, and O. Roustant. Finite-dimensional gauss-  
663 ian approximation with linear inequality constraints. *SIAM/ASA Journal of Uncertainty*  
664 *Quantification*, 6(3):1224–1255, 2018. doi: 10.1137/17M1153157.
- 665 R. A. Luettich, Jr. and J. J. Westerink. *Formulation and numerical implementation of the*  
666 *2D/3D ADCIRC finite element model version 44.XX*. ADCIRC.org, 2004. URL [https://adcirc.org/wp-content/uploads/sites/2255/2018/11/2004\\_Luettich.pdf](https://adcirc.org/wp-content/uploads/sites/2255/2018/11/2004_Luettich.pdf).
- 667  
668 H. Maatouk and X. Bay. Gaussian process emulators for computer experiments with in-  
669 equality constraints. *Mathematical Geosciences*, 49(5):557–582, 2017. doi: 10.1007/  
670 s11004-017-9673-2.
- 671 A. Neri, A. Bevilacqua, T. E. Ongaro, R. Isaia, W. P. Aspinall, M. Bisson, F. Flandoli,

- 672 P. J. Baxter, A. Bertagnini, E. Iannuzzi, S. Orsucci, M. Pistolesi, M. Rosi, and S. Vitale.  
673 Quantifying volcanic hazard at Campi Flegrei caldera (Italy) with uncertainty assessment:  
674 2. Pyroclastic density current invasion maps. *Journal of Geophysical Research: Solid Earth*,  
675 120(4):2330–2349, 2015. doi: 10.1002/2014JB011775.
- 676 A. K. Patra, A. C. Bauer, C. C. Nichita, E. B. Pitman, M. F. Sheridan, and M. I. Bursik.  
677 Parallel adaptive numerical simulation of dry avalanches over natural terrain. *Journal of*  
678 *Volcanology and Geothermal Research*, 139(1–2):1–21, 2005. doi: 10.1016/j.jvolgeores.2004.  
679 06.014.
- 680 A. Pensoneault, X. Yang, and X. Zhu. Nonnegativity-enforced Gaussian process regression.  
681 *Theoretical and Applied Mechanics Letters*, 10(3):182–187, 2020. doi: 10.1016/j.taml.2020.  
682 01.036.
- 683 E. B. Pitman, C. C. Nichita, A. K. Patra, A. C. Bauer, M. F. Sheridan, and M. I. Bursik.  
684 Computing granular avalanches and landslides. *Physics of Fluids*, 15(12):3638–3646, 2003.  
685 doi: 10.1063/1.1614253.
- 686 M. Plumlee, T. G. Asher, W. Chang, and M. V. Bilskie. High-fidelity hurricane surge fore-  
687 casting using emulation and sequential experiments. *The Annals of Applied Statistics*, 15  
688 (1):460–480, 2021. doi: 10.1214/20-AOAS1398.
- 689 C. A. Pope, J. P. Gosling, S. Barber, J. S. Johnson, T. Yamaguchi, G. Feingold, and P. G.  
690 Blackwell. Gaussian process modeling of heterogeneity and discontinuities using Voronoi  
691 tessellations. *Technometrics*, pages 1–20, 2019. doi: 10.1080/00401706.2019.1692696.
- 692 E. N. Rappaport. Fatalities in the United States from Atlantic tropical cyclones: New data  
693 and interpretation. *Bulletin of the American Meteorological Society*, 95(3):341–346, 2014.  
694 doi: 10.1175/BAMS-D-12-00074.1.
- 695 D. T. Resio and J. L. Irish. Tropical cyclone storm surge risk. *Current Climate Change*  
696 *Reports*, 1(2):74–84, 2015. doi: 10.1007/s40641-015-0011-9.
- 697 R. Rutarindwa, E. T. Spiller, A. Bevilacqua, M. I. Bursik, and A. K. Patra. Dynamic proba-  
698 bilistic hazard mapping in the Long Valley Volcanic Region, CA: Integrating vent opening  
699 maps and statistical surrogates of physical models of pyroclastic density currents. *Journal*  
700 *of Geophysical Research: Solid Earth*, 124(9):9600–9621, 2019. doi: 10.1029/2019JB017352.
- 701 J. Sacks, S. B. Schiller, and W. J. Welch. Designs for computer experiments. *Technometrics*,  
702 31(1):41–47, 1989a. doi: 10.1080/00401706.1989.10488474.
- 703 J. Sacks, W. J. Welch, T. J. Mitchell, and H. P. Wynn. Design and analysis of computer  
704 experiments. *Statistical Science*, 4(4):409–423, 1989b. doi: 10.1214/ss/1177012413.
- 705 L. Sandri, P. Tierz, A. Costa, and W. Marzocchi. Probabilistic hazard from pyroclastic density  
706 currents in the Neapolitan area (Southern Italy). *Journal of Geophysical Research: Solid*  
707 *Earth*, 123(5):3474–3500, 2018. doi: 10.1002/2017JB014890.
- 708 T. J. Santner, B. J. Williams, and W. I. Notz. *The Design and Analysis of Computer Experi-*  
709 *ments*. Springer Series in Statistics. Springer-Verlag, New York, NY, second edition, 2018.  
710 ISBN 978-1-4939-8845-7. doi: 10.1007/978-1-4939-8847-1.
- 711 J. Selva, W. Marzocchi, P. Papale, and L. Sandri. Operational eruption forecasting at high-  
712 risk volcanoes: the case of Campi Flegrei, Naples. *Journal of Applied Volcanology*, 1(5):  
713 1–14, 2012. doi: 10.1186/2191-5040-1-5.
- 714 E. T. Spiller, M. J. Bayarri, J. O. Berger, E. S. Calder, A. K. Patra, E. B. Pitman, and R. L.  
715 Wolpert. Automating emulator construction for geophysical hazard maps. *SIAM/ASA*

- 716 *Journal of Uncertainty Quantification*, 2(1):126–152, 2014. doi: 10.1137/120899285.
- 717 E. T. Spiller, R. L. Wolpert, S. E. Ogburn, E. S. Calder, J. O. Berger, A. K. Patra, and E. B.  
718 Pitman. Volcanic hazard assessment for an eruption hiatus, or post-eruption unrest context:  
719 Modeling continued dome collapse hazards for Soufrière Hills Volcano. *Frontiers in Earth*  
720 *Science: Geohazards and Georisks*, 8(535567):396, 2020. doi: 10.3389/feart.2020.535567.
- 721 M. L. Stein. *Interpolation of Spatial Data: Some Theory for Kriging*. Springer Series in  
722 Statistics. Springer Verlag, New York, New York, 1999.
- 723 R. Sulpizio, P. Dellino, D. M. Doronzo, and D. Sarocchi. Pyroclastic density currents: state  
724 of the art and perspectives. *Journal of Volcanology and Geothermal Research*, 283:36–65,  
725 2014. doi: 10.1016/j.jvolgeores.2014.06.014.
- 726 L. P. Swiler, M. Gulian, A. L. Frankel, C. Safta, and J. D. Jakeman. A survey of con-  
727 strained gaussian process regression: Approaches and implementation challenges. *Jour-*  
728 *nal of Machine Learning for Modeling and Computing*, 1(2):119–156, 2020. doi: 10.1615/  
729 JMachLearnModelComput.2020035155.
- 730 A. Taflanidis, J. Zhang, A. Kyprioti, A. Kennedy, and T. Kijewski-Correa. Developments in  
731 storm surge estimation using surrogate modeling techniques. *Coastal Engineering Proceed-*  
732 *ings*, (36v):currents.37, 2020. doi: 10.9753/icce.v36v.currents.37.
- 733 P. Tierz, E. R. Stefanescu, L. Sandri, R. Sulpizio, G. A. Valentine, W. Marzocchi, and A. K.  
734 Patra. Towards quantitative volcanic risk of pyroclastic density currents: Probabilistic  
735 hazard curves and maps around Somma-Vesuvius (Italy). *Journal of Geophysical Research:*  
736 *Solid Earth*, 123(8):6299–6317, 2018. doi: 10.1029/2017JB015383.
- 737 P. Tierz, B. Clarke, E. S. Calder, F. Dessalegn, E. Lewi, G. Yirgu, K. Fontijn, J. M. Crummy,  
738 Y. Bekele, and S. C. Loughlin. Event trees and epistemic uncertainty in long-term volcanic  
739 hazard assessment of rift volcanoes: The example of Aluto (Central Ethiopia). *Geochem-*  
740 *istry, Geophysics, Geosystems*, 21(10):e2020GC009219, 2020. doi: 10.1029/2020GC009219.
- 741 G. A. Valentine and M. R. Sweeney. Compressible flow phenomena at inception of lateral  
742 density currents fed by collapsing gas-particle mixtures. *Journal of Geophysical Research:*  
743 *Solid Earth*, 123(2):1286–1302, 2018. doi: 10.1002/2017JB015129.
- 744 V. Volodina and D. B. Williamson. Nonstationary Gaussian process emulators with kernel  
745 mixtures. *SIAM/ASA Journal of Uncertainty Quantification*, 8(1):1–26, 2020. doi: 10.  
746 1137/19M124438X.
- 747 X. Wang and J. O. Berger. Estimating shape constrained functions using Gaussian pro-  
748 cesses. *SIAM/ASA Journal of Uncertainty Quantification*, 4(1):1–25, 2016. doi: 10.1137/  
749 140955033.
- 750 W. J. Welch, R. J. Buck, J. Sacks, H. P. Wynn, T. J. Mitchell, and M. D. Morris. Screening,  
751 predicting, and computer experiments. *Technometrics*, 34(1):15–25, 1992. doi: 10.2307/  
752 1269548. URL <http://www.jstor.org/stable/1269548>.
- 753 J. J. Westerink, R. A. Luettich, J. C. Feyen, J. H. Atkinson, C. Dawson, H. J. Roberts,  
754 M. D. Powell, J. P. Dunion, E. J. Kubatko, and H. Pourtaheri. A basin-to channel-scale  
755 unstructured grid hurricane storm surge model applied to southern Louisiana. *Monthly*  
756 *Weather Review*, 136(3):833–864, 2008. doi: 10.1175/2007MWR1946.1.
- 757 K. Yang, V. Paramygin, and Y. P. Sheng. An objective and efficient method for estimating  
758 probabilistic coastal inundation hazards. *Natural Hazards*, 99(2):1105–1130, 2019. doi:  
759 10.1007/s11069-019-03807-w.

760 J. Zhang, A. A. Taflanidis, N. C. Nadal-Caraballo, J. A. Melby, and F. Diop. Advances  
761 in surrogate modeling for storm surge prediction: storm selection and addressing char-  
762 acteristics related to climate change. *Natural Hazards*, 94(3):1225–1253, 2018. doi:  
763 10.1007/s11069-018-3470-1.